

Characterizing arrhythmia using machine learning analysis of Ca^{2+} cycling in human cardiomyocytes

Jeremy K.S. Pang,^{1,2} Sabrina Chia,^{1,2} Jinqiu Zhang,³ Piotr Szyniarowski,³ Colin Stewart,³ Henry Yang,⁴ Woon-Khiong Chan,² Shi Yan Ng,^{5,6,7} and Boon-Seng Soh^{1,2,*}

¹Disease Modeling and Therapeutics Laboratory, A*STAR Institute of Molecular and Cell Biology, 61 Biopolis Drive Proteos, Singapore 138673, Singapore

²Department of Biological Sciences, National University of Singapore, Singapore 117543, Singapore

³A*STAR Skin Research Labs, 8A Biomedical Grove, Immunos, Singapore 138648, Singapore

⁴Cancer Science Institute of Singapore, National University of Singapore, Singapore 117599, Singapore

⁵Neurotherapeutics Laboratory, A*STAR Institute of Molecular and Cell Biology, 61 Biopolis Drive Proteos, Singapore 138673, Singapore

⁶Department of Physiology, Yong Loo Lin School of Medicine, National University of Singapore, Singapore 117456, Singapore

⁷National Neuroscience Institute, Singapore 308433, Singapore

*Correspondence: bssoh@imcb.a-star.edu.sg

<https://doi.org/10.1016/j.stemcr.2022.06.005>

SUMMARY

Accurate modeling of the heart electrophysiology to predict arrhythmia susceptibility remains a challenge. Current electrophysiological analyses are hypothesis-driven models drawing conclusions from changes in a small subset of electrophysiological parameters because of the difficulty of handling and understanding large datasets. Thus, we develop a framework to train machine learning classifiers to distinguish between healthy and arrhythmic cardiomyocytes using their calcium cycling properties. By training machine learning classifiers on a generated dataset containing a total of 3,003 healthy derived cardiomyocytes and their various arrhythmic states, the multi-class models achieved >90% accuracy in predicting arrhythmia presence and type. We also demonstrate that a binary classifier trained to distinguish cardiotoxic arrhythmia from healthy electrophysiology could determine the key biological changes associated with that specific arrhythmia. Therefore, machine learning algorithms can be used to characterize underlying arrhythmic patterns in samples to improve *in vitro* preclinical models and complement current *in vivo* systems.

INTRODUCTION

Prediction and prevention of arrhythmic events remains a global health concern. Despite improvements in risk assessment and management of cardiovascular events, manifestations of sudden cardiac death still account for 15%–20% of all deaths (Hayashi et al., 2015). There is an ongoing search for improved modeling platforms to identify aberrant electrophysiology and arrhythmia risk in healthy individuals exhibiting no heart conditions (Hayashi et al., 2015). In addition, improvements in the methodology to screen and identify cardiotoxicity in drugs is needed, as almost 10% of drugs within the past four decades were recalled from the clinical market because of cardiotoxicity not being detected in preclinical studies (Varga et al., 2015). The emergence of somatic cell reprogramming is paving the way to personalized medicine and disease-specific therapeutics (Oh et al., 2012). Assessment of cardiovascular health, sudden cardiac death risk, and cardiotoxicity screens can be done using human pluripotent stem cell-derived cardiomyocytes (hPSC-CMs) as opposed to limited primary cardiomyocyte (CM) tissues (Sallam et al., 2015). As such, adapting hPSC-CM systems to model electrophysiology will complement current clinical assessments in profiling risks among individuals in the population.

Current electrophysiological modeling systems are inherently mechanistic models whereby the causality be-

tween input and output parameters is studied in a hypothesis-driven manner (Baker et al., 2018). Genetic variations, cardiovascular structural defects, and chemical/drug exposure serve as the input parameters assessed for potential electrophysiological changes (Ch'en et al., 1998; Clancy and Rudy, 1999; Yap and Camm, 2003). Researchers analyze expected output parameters such as qualitative changes in action potential (AP) waveform, quantitative lengthening of AP duration, and repolarization duration, which are predictive of arrhythmia because of their association with QT interval prolongation and torsades de pointes (TdP) incidence to characterize electrophysiological changes (Fermini et al., 2015; Harris et al., 2013; Ma et al., 2011; Yap and Camm, 2003). However, there are limitations to these mechanistic models despite them being the fundamental workhorse of biological research. Preclinical assessment of drug cardiotoxicity, primarily via assessment of hERG channels for extended AP and repolarization durations, has been shown to be insufficient in capturing all forms of arrhythmogenesis (Fermini et al., 2015). Therefore, unbiased, *a priori* processing of electrophysiological data would help serve as a hypothesis-generating platform to identify unknown electrophysiological changes.

With the ease of generating large amounts of data, there has been a paradigm shift toward machine learning (ML) models (Baker et al., 2018; Kusumoto and Yuasa, 2019). Researchers carrying out hypothesis-driven research are



limited to probing empirically accepted subsets of input parameters, but ML models can take advantage of unbiased artificial intelligence to identify underlying patterns and generating correlations from broadly descriptive input parameters. We propose that a ML platform using electrophysiological data from *in vitro* cultures can be a complementary screening method to current clinical assessments to profile arrhythmic risk in individuals. In addition, the unbiased ML models can identify the key electrophysiological alterations due to arrhythmic treatments for further mechanistic analysis.

Three established methods exist to generate electrophysiological data suitable for ML model training: patch clamping, multi-electrode arrays (MEAs), and fluorescence reporter tracking of Ca^{2+} transients (Fermini et al., 2015; Jiang et al., 2018; Ma et al., 2011). Differences in the form of electrophysiological data generated have led us to prefer Ca^{2+} transient analysis over the other two approaches. Although patch clamping is widely considered as the gold standard for ion channel research, its relatively low throughput and requirement for highly trained personnel limits its ability to generate the large, high-quality datasets. Automated patch-clamp systems could alleviate both limitations and enable higher throughput data generation (Ma et al., 2011). However, these high-end systems are not commonplace and may not be readily available for use by researchers. The MEA system is also suitable to build a high-throughput analysis platform on, with multiple electrodes probing many cells concurrently. However, we experienced that individual electrodes would often be in contact with multiple CMs, resulting in confounding data when asynchronously contracting arrhythmic CMs were analyzed. This limitation can be controlled for when probing for single CMs using Ca^{2+} transient analysis. Last, mature CMs used for both MEA and patch-clamping systems must be dissociated and replated onto suitable plates or slides for analysis. This replating process is not physiological and would likely cause unintended restructuring of cytoskeletal elements and the development of arrhythmic properties. Fluorescent analysis of Ca^{2+} transients does not require replating and thus is not subject to this confounding factor.

Conversely, both patch clamping and MEA are more versatile in generating electrophysiological data compared with the limited nature of Ca^{2+} transient analysis, probing only for perturbations of Ca^{2+} handling. It is plausible that electrophysiological data for the various ion channel types and field potential could generate better models. However, as the cycling of intracellular Ca^{2+} ions is the primary regulator enabling the rhythmic cardiac cycles, probing the Ca^{2+} cycling capabilities alone could suffice as a proxy for electrophysiological health (Bers, 2001). Tracking of the Ca^{2+} transients in CMs can be done non-invasively

through fluorescence imaging systems readily available in biological labs.

In this study, hPSC-CMs expressing the Ca^{2+} reporter GCaMP6s were derived using an established protocol to generate electrophysiology data (Lian et al., 2013). We developed a Ca^{2+} reporter image analysis pipeline that tracks the Ca^{2+} cycling of CMs at the single-cell level, followed by decomposition of the recorded Ca^{2+} transient waveforms into 16 Ca^{2+} handling parameters to be used as inputs to train ML classifiers (Figure 1A). Three experimental groups containing healthy CMs and CMs of arrhythmic subtypes were pooled into a cohort ($n = 3,003$), and their Ca^{2+} handling parameters were used as inputs to train four multi-class classifiers to distinguish between healthy CMs and the various arrhythmic subtypes (Figure 1B; Table 1). To identify key features of arrhythmogenesis for specific arrhythmic subtypes, we trained binary classifiers using data within experimental groups, between the healthy CMs and arrhythmic CM subtypes, to determine if the expected biological parameters were used to determine arrhythmogenesis (Figure 1C). The algorithms used to construct this are made accessible to enable other users to similarly dissect and analyze their datasets.

RESULTS

Ca²⁺ transients of CMs can be tracked at the single-cell level for arrhythmia risk assessment by stable expression of Ca²⁺ reporter GCaMP6s

Although Ca^{2+} transients can be tracked with Ca^{2+} fluorophores, treatment with the fluorophores is toxic and must be done as an endpoint experiment. Thus, we opted to stably express the genetically encoded Ca^{2+} indicator GCaMP6s, which allows tracking of Ca^{2+} cycling at single-cell resolution in CMs over multiple time points. Thus, GCaMP6s was inserted into and expressed in the hPSC lines (H7 ESCs, BJ induced pluripotent stem cells [iPSCs], Hutchinson-Gilford progeria syndrome [HGPS] iPSCs) used in this study using CRISPR (Figures S1A and S1B) (Jiang et al., 2018). Fluorescence was used as a preliminary screen for hPSC knockin, with successful GCaMP6s insertions resulting in a faint detectable green fluorescence in hPSCs (Figure S1C). PCR genotyping was used to screen for homozygous insertions (Figure S1D). Several studies have highlighted incidences of deleterious, unwanted on-target insertions and deletions from CRISPR gene editing that escape conventional PCR and Sanger sequence analysis (Shin et al., 2017). Therefore, the lines generated for this work were validated to be free of unwanted mutations by first probing for fragments of the donor plasmid (Figures S1E and S1F). In addition, quantitative genotyping PCR (qgPCR) was also carried out to confirm that the lines

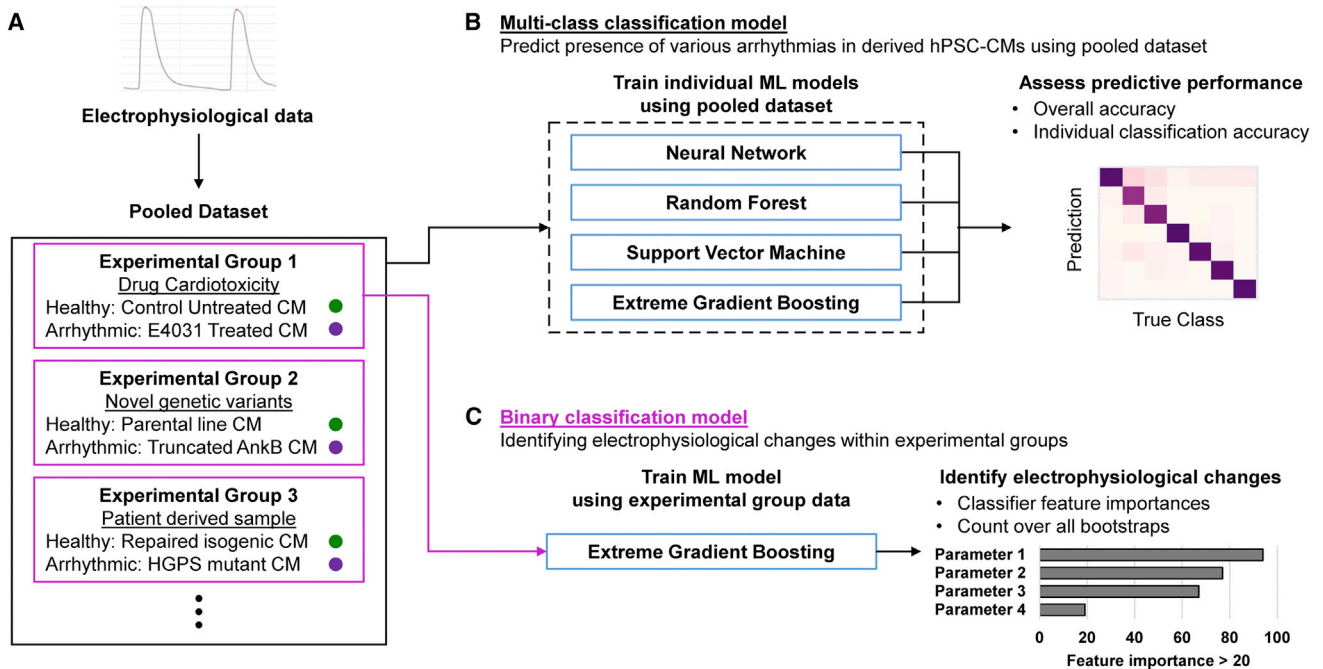


Figure 1. Framework to train machine learning algorithms to predict arrhythmogenesis and identify electrophysiological changes

(A) Single-cell CM Ca^{2+} cycling is tracked and processed to obtain the electrophysiological data contained within experimental groups containing specific arrhythmic forms.

(B) For a multi-class arrhythmia prediction model, the pooled dataset is split into multiple train-test splits to train 4 different ML models over 100 bootstraps to identify the best consistently performing ML classifier.

(C) Binary classification models are trained using individual experiment groups containing a healthy CM class and the arrhythmic CM subclass of interest. Assessing the feature importance metric of the trained classifiers can deduce the biological implications of the arrhythmic subclass studied to enable targeted therapy.

were indeed homozygous and not false positives (Figure S1G) (Simkin et al., 2022).

After clonal isolation of hPSC^{GCaMP6s+/+} lines, pluripotency maintenance was confirmed by qRT-PCR for pluripotency genes (Figure S2A). As there have been reports on the cell toxicity of GCaMP, karyotyping was also carried out for hPSC^{GCaMP6s+/+} lines (Figure S2B) (Tallini et al., 2006). To ensure that the CMV-driven GCaMP6s does not undergo gene silencing over long-term cultures, the hPSC^{GCaMP6s+/+} lines were probed for *GCaMP6s* gene expression levels (Brooks et al., 2004). No significant changes in gene expression levels were found between early (passage <10) and late (passage ~30) hPSC^{GCaMP6s+/+} lines (Figure S2C). In addition, quantification of the fluorescent intensity of individual hPSC colonies in Ca^{2+} containing media also showed no significant changes between early and late passages (Figure S2D). In this work, to prevent any confounding effects of CMV promoter silencing, hPSC^{GCaMP6s+/+} lines were differentiated within 20 passages of clonal isolation.

Directed differentiation toward the CM lineage was achieved using an established protocol (Figure S2E) (Lian et al., 2013). Metabolic selection and maturation was car-

ried out using a previously established protocol, via treatment with glucose-free, fatty acid supplemented media, resulting in a >90% pure population of CMs (Figure S2F) (Correia et al., 2017). Fluorescent videos confirmed visual tracking of CM contraction cycles (Figure 2A; Videos S1 and S2). Individual CMs were identified as regions of interest (ROIs), and their fluorescent intensity representing their Ca^{2+} cycling was quantified over the duration of the recordings (Figure 2B). All CM Ca^{2+} fluorescent intensity over time data generated in this study were recorded in this manner for downstream analysis.

Input parameters can be derived by decomposing Ca^{2+} fluorescent intensity over time data from cardiomyocytes at single-cell resolution

After video analysis of each individual CM as an ROI, the fluorescent intensity over time data generated was processed to summarize the Ca^{2+} cycles into parameters that describe the CM electrophysiology. The Ca^{2+} signal of each CM was processed frame by frame to identify fluorescent peaks corresponding to systole. Peaks are algorithmically identified on the basis of three criteria: (1) the absolute



Table 1. Classifications of healthy and arrhythmic CMs from the three independent experimental groups generated

Experimental groups	Sample name/treatment	Classification	Sample size
Drug-induced arrhythmia	BJ-CM/DMSO control	Healthy	178
	BJ-CM/10 μ M E4031	10 μ M E4031: Arrhythmic	173
	BJ-CM/40 μ M E4031	40 μ M E4031: Arrhythmic	169
Ankyrin-B syndrome	H7-CM	Healthy	596
	H7-CM/ANK frameshift 1	Mut A1: Arrhythmic	409
	H7-CM/ANK frameshift 2	Mut A2: Arrhythmic	642
	H7-CM/ANK frameshift 3	Mut A3: Arrhythmic	274
Progeria syndrome	HGPS-CM	Mut HGPS: Arrhythmic	120
	Isogenic HGPS-CM/LMNA mutation repaired	Healthy	211
	BJ-CM	Healthy	231

fluorescent intensity at the peak is a local maximum; (2) there is a time point prior to the peak with a first-order differential above a threshold, corresponding to the start of a single depolarization; and (3) the absolute fluorescent intensity at that peak is above a specified threshold, to prevent minor fluctuations from fluorescent minima from being detected as peaks (Figure 2C). These Ca²⁺ peaks detected represent individual Ca²⁺ transients.

The following parameters regarding each individual Ca²⁺ transient were computed using information of the depolarization initiation point corresponding to the initiation of systole, the Ca²⁺ peak corresponding to the maximum contraction point of systole, and the corresponding fluorescent minima corresponding to diastole (Figure 2C; Table S1). These parameters are analogous to that of AP duration and field potentiation duration changes in patch clamping or multi-electrode array models, respectively, used in preclinical safety assays (Dempsey et al., 2016; Harris et al., 2013):

1. Beat-to-beat duration, the time between one Ca²⁺ transient peak and the next.
2. Depolarization duration, the time between the first-order derivative maximum and the fluorescent peak.
- 3–5. Repolarization durations 30%, 60%, and 90%, the times between the fluorescent peak and 30%, 60%, and 90% reduction of fluorescence intensity.

6. Calcium transient duration (CTD), the time between the first-order derivative maximum and the 90% repolarization time point.

In addition to these 6 absolute variables, the following normalizations of some of these absolute variables into compound variables were performed to further describe each Ca²⁺ waveform (Table S2):

7. CTD normalized to beat-to-beat duration (CTDNB).
8. Depolarization duration normalized to CTD (DepolarizationNCTD).
9. Repolarization 30% normalized to repolarization 90% (Repolarization30NR90).

These 9 parameters were computed across all Ca²⁺ transients in each single-cell recording. The mean of these 9 parameters together with the SDs of 7 of these parameters were computed to obtain 16 parameters in total to summarize the Ca²⁺ handling properties of each individual CM. The SDs of repolarization duration 30% and repolarization duration 60% were excluded, as these parameters are highly similar to the SD of the included repolarization duration 90%. Theorized molecular explanations pertaining to the means and SDs of these defined parameters are described at length in Tables S3 and S4. Figure 2D details the process of obtaining electrophysiological parameters to be used as ML inputs for a single experimental group containing both healthy and arrhythmic subtype CMs.

Generation of three experimental groups containing healthy and arrhythmic CMs covering various arrhythmic forms

Studying a particular arrhythmic subtype requires a comparison between healthy CMs and their arrhythmic equivalent CMs. Building a ML risk prediction platform by pooling independent experimental groups in a modular manner will facilitate studying other forms of arrhythmia from external datasets. Thus, three independent experimental groups composed of healthy CMs and their equivalent arrhythmic CMs were generated for this proof-of-concept work. These three arrhythmogenic sources were all expected to confer a bradycardic effect on the CMs, albeit with a different underlying mechanism. Ca²⁺ handling parameters of CMs from each experimental group were obtained by decomposing their Ca²⁺ transients into the 16 parameters described above and used as ML inputs (Data S1).

The first experimental group explores effects of drug-induced arrhythmogenicity using E4031, a known cardiotoxic agent that blocks the I_{Kr} repolarization current previously used to model long-QT syndrome (Harris et al., 2013). Previously studied as a possible anti-arrhythmic agent, E4031 exerts a slowdown of the cardiac contraction cycle

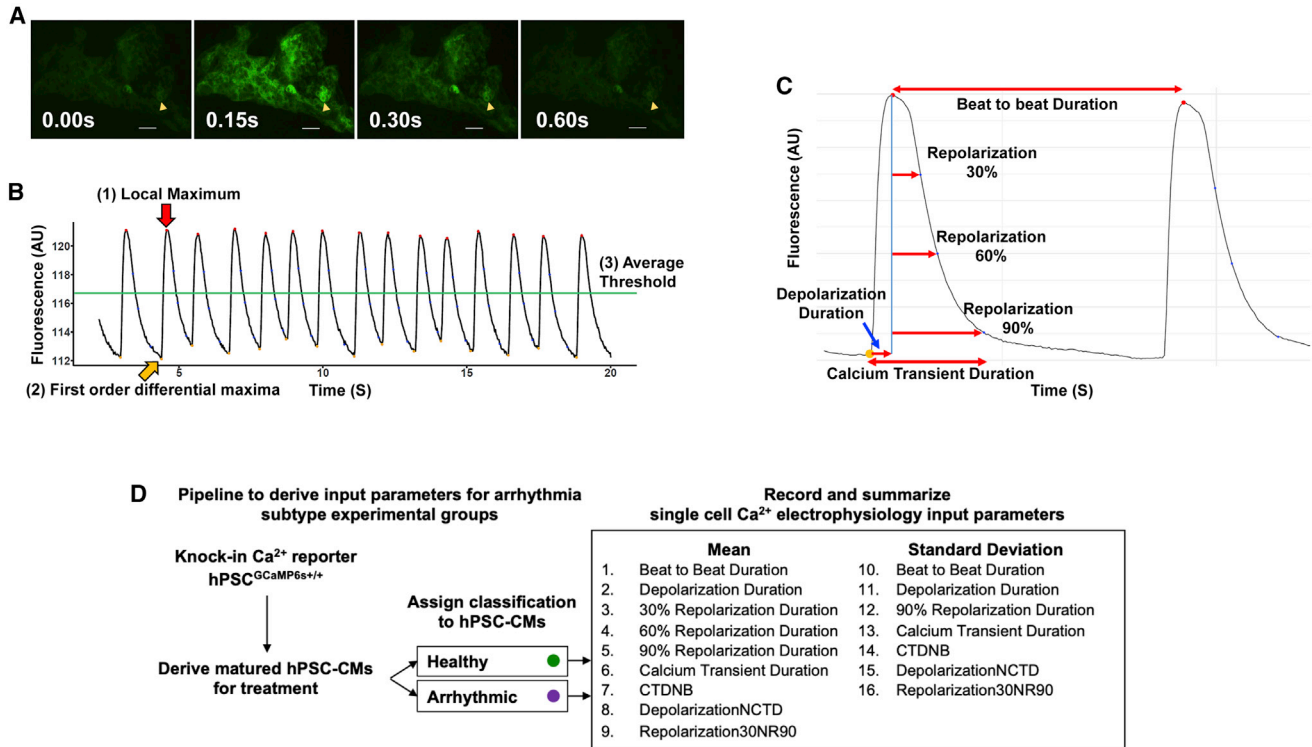


Figure 2. Functional validation of GCaMP6s Ca²⁺ reporter by breaking down of Ca²⁺ cycling readout into biological parameters (A) Single frame of a video tracking BJ-CM Ca²⁺ cycling. The arrow marks a single CM ROI tracked. Scale bar, 50 μ m. (B) Fluorescence over time plot of a single CM. Identification of fluorescence peaks such as (1) was automated using the three criteria described. (C) Annotation of individual Ca²⁺ transient parameters. Each parameter is computed for every detected Ca²⁺ transient peak and summarized across the entire Ca²⁺ cycling readout from a single CM video recording. (D) Flowchart highlighting the process to generate the electrophysiological data representing the healthy and arrhythmic Ca²⁺ waveforms in a singular experimental group. Each CM is represented by either healthy or an arrhythmic subtype classification and 16 Ca²⁺ handling parameters.

and can be used to prevent tachycardias (Adaniya and Hiraoaka, 1990). Healthy BJ iPSC-derived CMs (BJ-CMs) were treated with two concentrations of E4031 (10 μ M E4031, n = 173; 40 μ M E4031, n = 169) for 2 h and compared with DMSO control (Ctrl; n = 178) treatment (Data S2). Two concentrations of E4031 were used to demonstrate dose effects of the drug-induced arrhythmogenesis.

The second experimental group explores the arrhythmogenic effect of mutation at the ANK2 gene locus encoding for Ankyrin-B (AnkB), generated *in vitro* via CRISPR-directed mutagenesis. AnkB plays a crucial role in localizing and stabilizing a range of membrane ion channels necessary for Ca²⁺ cycling in human CMs and is implicated in Ankyrin-B syndrome, which presents with a spectrum of rhythmic irregularities including alternating bradycardia and tachycardia (Cunha and Mohler, 2006; Le Scouarnec et al., 2008). The Cas9 was targeted to exon 40 coding for the death domain, which has mutations linked with abnormal cardiac function (Ichikawa et al., 2016)

(Figure S3A). Three biallelic frameshift mutants with truncated AnkB expression were generated, henceforth termed Mut A1, Mut A2, and Mut A3 (Figures S3B–S3D; Table S5). On the basis of flow cytometry, the Mut A1 and Mut A2 lines achieved similar differentiation efficiency compared with the parental H7 embryonic stem cell (ESC) line, while the A3 line exhibited poorer differentiation efficiency (Figure S3E). Western blot confirmed that AnkB expression is lost in A1 and A3 CMs but expressed at a reduced level for A2 CMs (Figure S3F), and all three mutant lines exhibited significant reduction in cardiomyocyte marker *TNNT2* expression (Figure S3G). The Ca²⁺ handling parameters of these three AnkB mutant lines (Mut A1, n = 409; Mut A2, n = 642; Mut A3, n = 274) were compared with the parental H7 ESC-derived CMs (H7-CMs; n = 596) (Data S3).

The third experimental group explores electrophysiological changes present in patients afflicted with congenital Hutchinson-Gilford progeria syndrome. HGPS most

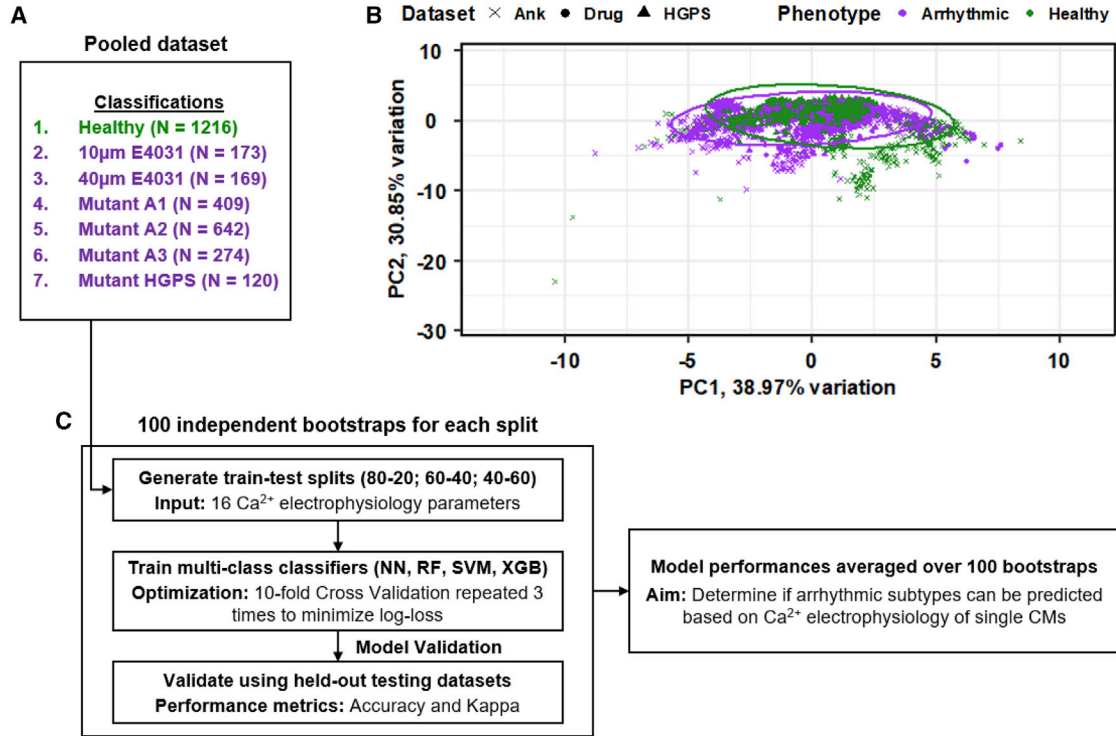


Figure 3. Healthy and arrhythmic CMs could not be separated on a linear principal-component analysis

(A) Pooled dataset containing the healthy classification and the six different arrhythmic subclasses from the three experimental groups used in this study.

(B) First two PCs depicting the healthy and arrhythmic CMs and their associated datasets, accounting for 69.8% of variation present. Colors correspond to the arrhythmic/healthy classification. Symbols correspond to the associated datasets.

(C) Overall workflow to identify the most consistent ML classifiers trained on the multi-class pooled dataset and the optimal train-test split to prevent overfitting.

commonly occurs because of a single base pair substitution (C1824T, p.G608G) within exon 11 of the lamin A/C gene, *LMNA*, creating a cryptic splice site leading to the accumulation of a truncated protein termed Progerin. HGPS results in premature death occurring primarily in the second decade of life because of cardiovascular complications (Hennekam, 2006). As HGPS is an ultrarare condition, extensive clinical research is lacking, but cardiac abnormalities including bradycardia and PQ interval/QRS complex prolongation likely contributing to premature death have been demonstrated in progeroid mice (Rivera-Torres et al., 2016). Previously, an iPSC line together with its corrected isogenic control was reprogrammed from a HGPS patient fibroblast carrying the heterozygous point mutation (Zhang et al., 2011) (Figure S4A). Western blot of derived CMs validated the absence of Progerin in the isogenic line (Figure S4B). The Ca²⁺ handling parameters of both the mutant (Mut HGPS; n = 120) and isogenic (Iso HGPS; n = 211) iPSC-CMs were assessed and compared with a healthy BJ CM control (BJ-CMs; n = 231) cultured together with the HGPS lines (Data S4). Several electrophysiological

parameters of the Iso HGPS line improved and were comparable with the healthy BJ-CM control, particularly the mean and variation of both beat-to-beat duration and the CTDNB ratio, a parameter indicative of the refractory period of the CMs (Figure S4C).

Healthy and arrhythmic CMs are not linearly distinguishable on the basis of their electrophysiological parameters

To highlight the basis for applying a ML approach to distinguish between healthy and arrhythmic CMs, all three experimental groups were pooled together into a combined dataset representing healthy cells of different origins, as well as CMs experiencing various forms of arrhythmias (Figure 3A). In the pooled dataset, all the healthy CM lines (Ctrl BJ-CMs, H7-CMs, Iso HGPS, and BJ-CMs) were classified as “Healthy,” while the arrhythmic CMs maintain their arrhythmic subtype classification (Table 1). An unsupervised linear transformation of the electrophysiological parameters defining the CMs using principal-component analysis (PCA) was unable to clearly separate the healthy



CMs from arrhythmic classes from each dataset (Figure 3B). Scree plot analysis of the PCA shows that 90% of the variation present in the parameters can be explained using 5 principal components (PCs), but a pairwise relationship plot revealed no obvious distinction between healthy CMs from arrhythmic CMs within these 5 PCs (Figure S5). Therefore, as CMs in a healthy state or an arrhythmic state could not be linearly separated on the basis of their electrophysiological parameters, a more complex, computational approach is warranted.

Machine learning classifiers can accurately classify various arrhythmogenic CMs by training on the multi-class pooled dataset

To improve on the separation of healthy CMs from the arrhythmic CMs, four ML algorithms were adapted as multi-class classifiers: neural network (NN), random forest (RF), support vector machine radial kernel (SVM), and extreme gradient boosting (XGB). These four classifiers were trained in parallel using 16 different parameters previously defined (Tables S3 and S4).

The pooled dataset depicted in Table 1, with the 7 classifications (Healthy, 10 μ M E4031, 40 μ M E4031, Mut A1, Mut A2, Mut A3, and Mut HGPS) were partitioned into train-test splits. Three different train-test ratios were tested (80:20, 60:40, and 40:60), and 100 independent bootstraps were analyzed for each ratio. The performance of the optimized model was assessed using the held-out testing dataset within each bootstrap by computing the accuracy and kappa metrics. Two classification methods were tested, an individualized prediction strategy and a majority voting prediction strategy. For the individual prediction strategy, if the predicted classification of a single CM electrophysiology matches that of its actual classification, the prediction is considered accurate. For the majority voting prediction strategy, all CMs recorded within the same ROI were considered to be from the same individual, and the most common predicted classification across the CMs was determined as the majority. The majority prediction is then used in place of all other predictions of the CMs within the ROI. Figure 3C summarizes the flow of the data analysis, from generation of each independent bootstrap split to the overall analysis of ML classifier performances.

Comparison between the overall performance of the four ML models revealed that the classic SVM algorithm significantly underperformed compared with the other algorithms, achieving only 50%–55% accuracy in classifying unseen test data regardless of train-test splits or prediction strategy (Figure 4A). The main reason behind this underperformance is likely that the base SVM algorithm is a pairwise binary classifier, and its ability to do multi-class classification is an extension of doing multiple pairwise

comparisons. Across the remaining three algorithms, the majority voting strategy has a clear performance advantage compared with the individual prediction strategy across all train-test splits (Figure 4B). However, at the 80:20 train-test split, the XGB classifier performed only marginally better than the 60:40 train-test split, while the NN and RF classifiers both performed slightly poorer, a sign of overfitting. This overfitting does not occur even with an 80:20 train-test split for all three classifiers in the individual prediction strategy (Figure 4B). Overall, these results suggest that the XGB classifier is more robust compared with the other ML classifiers in predicting the presence of arrhythmogenesis and is also more resistant to overfitting data as well.

Assessing the individual classification accuracy of the 60:40 split XGB model, the majority voting strategy outperforms the individual prediction strategy in sensitivity (Figure 4C). Consequently, the F1 score, a performance metric accounting for both sensitivity and specificity of the model, is also higher for the majority voting strategy. Notably, the trained models are less sensitive to the presence of E4031 drug treatment. The heatmaps depicting the confusion matrices across all 100 bootstraps highlight the fact that most prediction errors within the drug treatment classes are mislabeled into the “Healthy” class (Figure 4D). A plausible explanation for this phenomenon is that not all CMs within the treated datasets were equivalently affected by E4031, resulting in some CMs exhibiting electrophysiology close to their healthy CM equivalents. In agreement with this hypothesis, there is an observable dose dependence effect, as the XGB classifiers were more sensitive to the presence of the higher 40 μ M of arrhythmogenic E4031 drug treatment (88%) as opposed to the lower 10 μ M treatment (75%). Therefore, the XGB classifier can predict arrhythmic risk within these seven subclasses accurately and could potentially differentiate between extents of arrhythmogenesis by assessing its ability to train and perform between classes.

Binary machine learning classifiers distinguish between healthy and arrhythmogenesis using biologically appropriate parameters

To further explore the hypothesis that ML classifiers can classify CMs into various arrhythmic risk categories while considering various extents of arrhythmogenesis, we assessed if these models were grounded in biological basis to make their predictions. Biologically appropriate ML models can be used for patient-specific therapy, providing a hypothesis-generating platform to identify key underlying electrophysiological changes attributed to arrhythmogenic conditions as opposed to classical arrhythmia models whereby only changes in TdP-inducing parameters are considered. The biological appropriateness of the trained

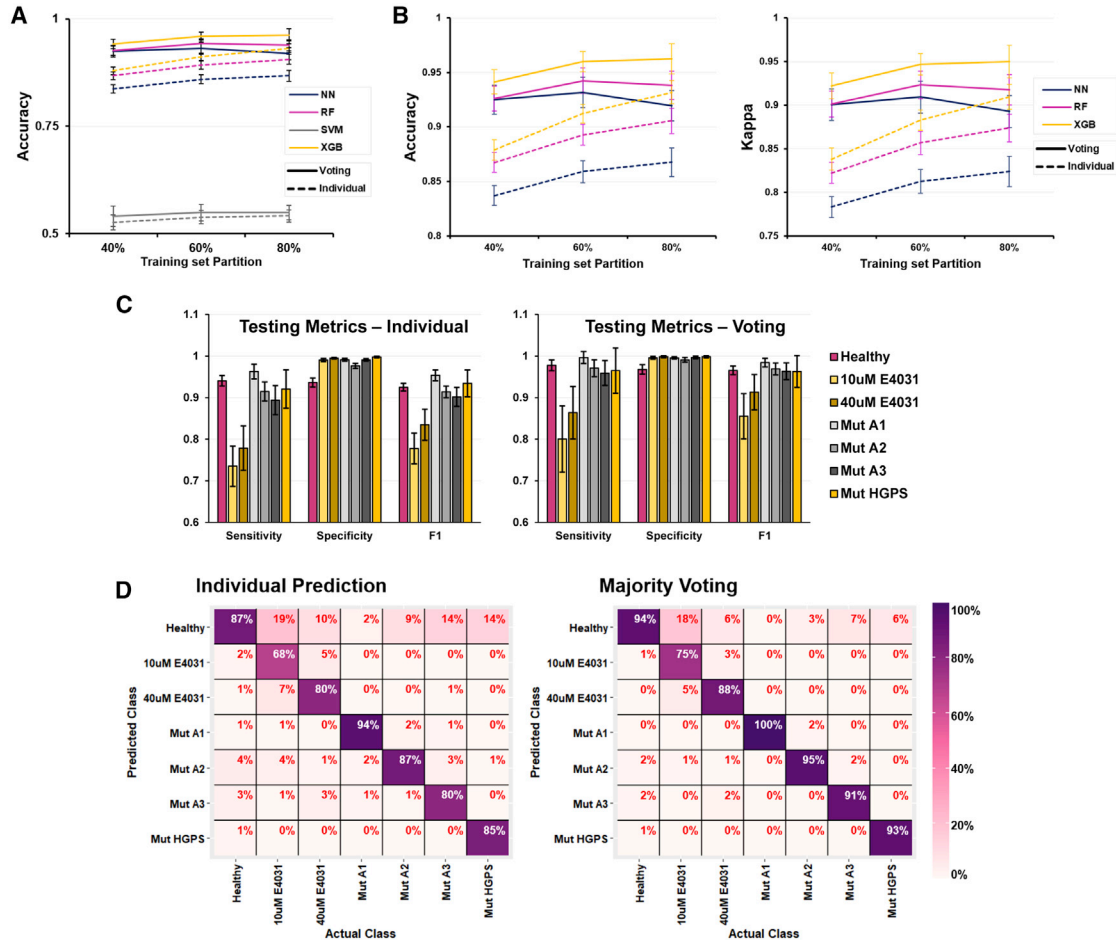


Figure 4. ML algorithms used to build the multi-class prediction model performed well despite no distinct separation detected from principal-component analysis

(A) Accuracy of all four trained multi-class classification models on the held-out testing datasets. Dashed lines, individual prediction strategy; solid lines, majority voting strategy.

(B) Accuracy and kappa metrics focusing on the three better performing multi-class classification models on the held-out testing datasets.

(C) Sensitivity, specificity, and F1 scores of the XGB multi-class classification models assessed using the held-out testing datasets. Left: individual prediction strategy. Right: majority voting strategy.

(D) Confusion matrixes of the XGB models assessed using the held-out testing datasets. The horizontal axis is the true classification of the CM test data, while the vertical axis is the XGB model predicted classification. Prediction errors fall within the column of the true classifications. Left: individual prediction strategy. Right: majority voting strategy. Mean \pm SD is plotted for $n = 100$ independent bootstraps for all figures.

models can be determined by probing the features they consistently use highly using the feature importance metric. However, there is little relevance in assessing the feature importance metric in the multi-class prediction model, as each arrhythmic class has differing underlying causes and alterations in the electrophysiology. Even in the selected bradycardic arrhythmias used in this study, apart from an expected increase in beat-to-beat duration, the underlying alterations in electrophysiology might be different. Therefore, training binary classifiers to compare

healthy and individual arrhythmic subclasses is necessary to determine if ML models are using features in a biologically appropriate manner.

Within the datasets studied, the E4031 drug-induced arrhythmogenesis experimental group is the most appropriate to assess biological relevance of ML models, as the induced arrhythmogenesis has a known phenotype. It has been reported that the primary arrhythmogenic effect of E4031 is the lengthened repolarization duration due to the blockage of the I_{Kr} repolarization current (Harris

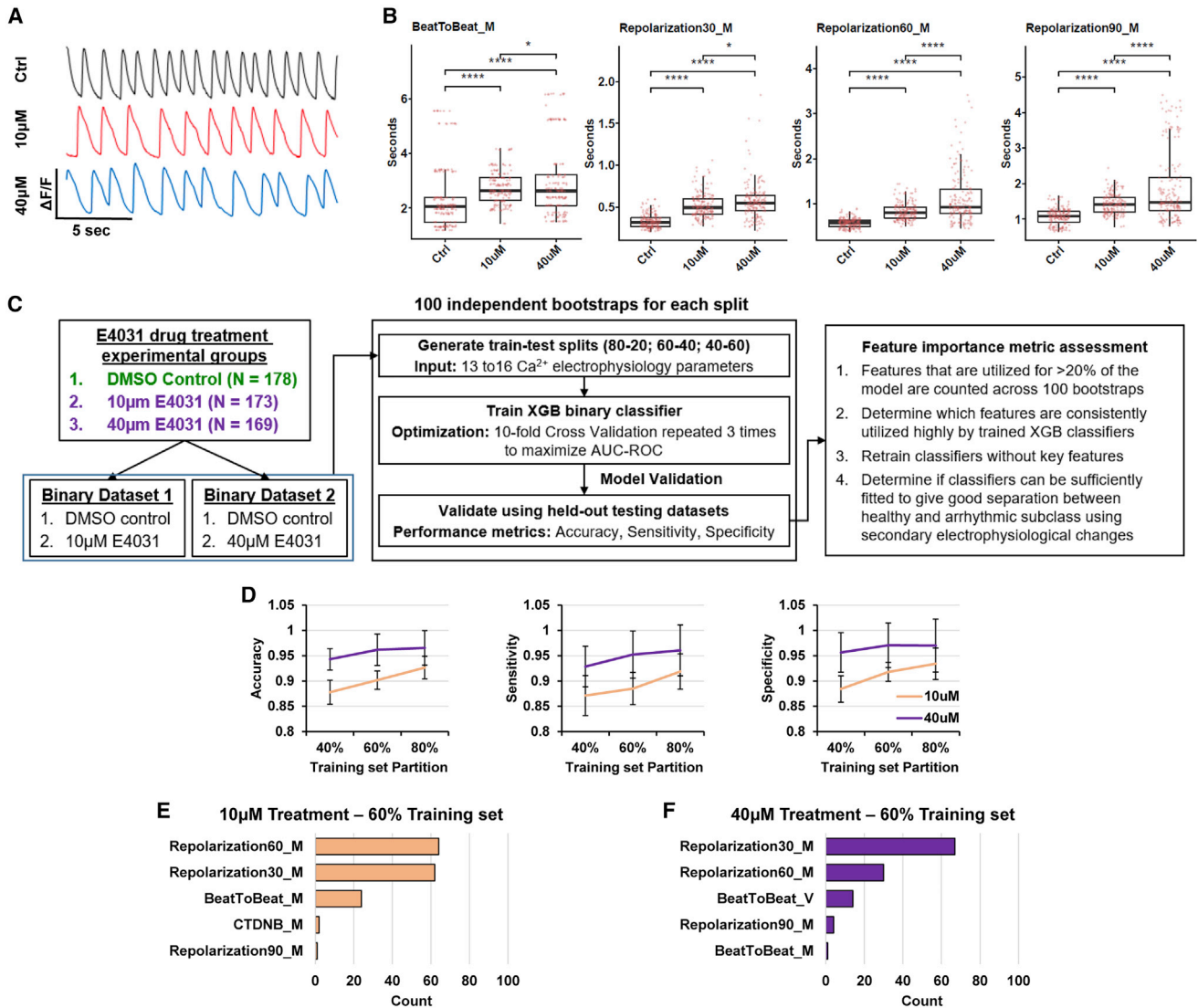


Figure 5. Biological changes due to drug-induced arrhythmogenesis are captured by machine learning classifiers

(A) Representative Ca²⁺ cycling plots depicting qualitative changes in Ca²⁺ transients.

(B) Boxplots depicting quantitative comparison across treatment groups for beat-to-beat duration (BeatToBeat_M) and 30%, 60%, and 90% repolarization duration parameters (Repolarization30_M, Repolarization60_M, and Repolarization90_M, respectively). Each point represents a single CM. **p* < 0.05 and *****p* < 0.0001; two-tailed Student's *t* test. Ctrl, 10 µM, 40 µM plotted with *n* = 178, 173, 169 CMs respectively.

(C) Overall workflow to validate that XGB classifiers use biologically appropriate features to determine arrhythmogenesis. XGB classifiers were trained on the two drug treatment binary datasets on three train-test splits, and their feature importance was determined.

(D) Performance metrics of the XGB binary classifiers assessed using the held-out testing datasets. Left: accuracy. middle: sensitivity. Right: specificity. Mean ± SD is plotted for *n* = 100 independent bootstraps for all figures.

(E and F) Total count of all parameters that scored >20 on the feature importance metrics across all XGB model bootstraps of the (E) 10 µM E4031 treatment dataset and the (F) 40 µM E4031 treatment dataset at a 60:40 train-test split.

et al., 2013). Visualizations of the Ca²⁺ transients show alterations in the waveforms in the 10 µM drug-treated CMs compared with the healthy control CMs, with a more severe effect observed in the higher 40 µM treatment group (Figure 5A). Quantification of the Ca²⁺ transient param-

eters confirms the lengthened repolarization durations, as well as a significant reduction in contraction speed attributed to the bradycardic effect of E4031 (Figure 5B). Therefore, both concentrations of E4031 exert the expected biological phenotype known to cause arrhythmogenesis in



CMs, and the higher dosage does result in a more severe phenotype.

To validate if the XGB classifiers would use the extended repolarization duration as features to predict E4031-induced arrhythmogenesis, both drug-treated datasets were used to generate binary XGB classifiers (Figure 5C). Similar to the multi-class prediction model, each binary dataset was split evenly across the classes into three train-test splits (80:20, 60:40, and 40:60) for 100 independent bootstraps. Across the train-test splits, the trained XGB classifier consistently performed better in classifying the higher dosage treatment (Figure 5D). Accuracy peaked at 60:40 train-test splits for 40 μM treatment (96.1%), while still marginally improving from 90.2% to 92.7% when increasing to 80:20 for 10 μM treatment. These results agree with the prior multi-class analysis, with 60:40 train-test split being optimized without overfitting and highlighting that the XGB classifiers are sensitive to dose effects and can more accurately predict the presence of higher 40 μM arrhythmogenic drug treatment than the lower 10 μM treatment.

Furthermore, we assessed the feature importance metric across each of the 100 independent models trained to classify the drug-treated CMs. Classifiers trained on the 60:40 train-test splits to distinguish the 10 μM treatment group used the 30% and 60% repolarization duration parameters highly, with >60 bootstraps using these parameters at >20% of the model (Figure 5E). A similar conclusion can be drawn from the classifiers trained to predict the 40 μM treatment group, with 67 and 30 bootstraps using repolarization 30% duration and 60% duration at >20% of the model respectively (Figure 5F). Changing the train-test ratios resulted in classifiers still consistently using either repolarization 30% and 60% duration parameters, suggesting a strong correlation between the extended repolarization duration and electrophysiological changes of the E4031 arrhythmic subclass (Figure S6). As the basic Ca^{2+} transient analysis did confirm the expected lengthening of Ca^{2+} repolarization duration due to E4031 treatment, the trained ML classifiers are biologically appropriate by using repolarization duration as the main feature distinguishing the drug-treated group from the healthy CMs. In addition, the prolongation of repolarization of E4031 consequently slows the cardiac contraction rhythm and increases beat-to-beat duration (Adaniya and Hiraoka, 1990). These findings agree with the lengthened beat-to-beat duration feature also consistently used by models across the various train-test splits to distinguish between healthy and E4031-treated CMs, strongly correlating the expected bradycardic phenotype to the electrophysiological changes of the E4031-treated arrhythmic subclass.

Next, we assessed whether the repolarization duration features could be replaced by the other electrophysiological

features input into the model. XGB models were trained at the same 60:40 train-test splits without the repolarization 30% and 60% duration parameters. As expected, the top features used to generate the models became the extension of CTD and repolarization 90% duration (Figure 6A, top). CTD is made up of the depolarization duration and the repolarization 90% duration, and thus it would be the next likely feature that separates healthy CMs and E4031-treated CMs, alongside the repolarization 90% duration feature itself. Removal of the repolarization 90% duration then resulted in models using the increased CTD and beat-to-beat duration, which, as previously mentioned, are the expected secondary electrophysiological changes of the E4031-treated arrhythmic subclass (Figure 6A, bottom). Interestingly, there is no loss in model performance when these repolarization features are removed, suggesting that the secondary electrophysiological changes can sufficiently capture the E4031 treatment arrhythmic phenotype (Figure 6B). Therefore, these results confirm that the trained XGB classifiers are using the key biological changes to distinguish between healthy and the E4031-treated arrhythmic subclass.

DISCUSSION

In the field of arrhythmia modeling, there has been increasing interest in ML, with a few recent publications using trained ML models to study CM electrophysiology (Golgooni et al., 2019; Hwang et al., 2020; Juhola et al., 2015). These previous works highlight how single ML classifiers can be trained by the classifications of experienced researchers to accurately determine abnormal FPD or Ca^{2+} transients. In this work, we further showcase the utility of artificial intelligence in arrhythmia modeling, laying the groundwork by demonstrating that ML classifiers can be trained using single-cell, decomposed Ca^{2+} transients of CMs derived from both healthy and arrhythmic origins to predict the presence of the specific arrhythmias without any expert intervention. In addition, we show that the binary ML classifiers do use biologically appropriate parameters to make predictions and thus can be used in an unbiased manner to identify key electrophysiological changes due to unknown novel treatments.

The current scope of the developed ML classifiers are limited to the three forms of arrhythmia with bradycardia implications, but with the high accuracy rate (>90%) in identifying arrhythmic CMs using the majority voting strategy, there is confidence to adapt and pool in additional experimental groups for larger scale application. Currently, there is no available database storing electrophysiological data from CMs. Thus, the main limitation of the arrhythmia prediction platform would be to scale up the

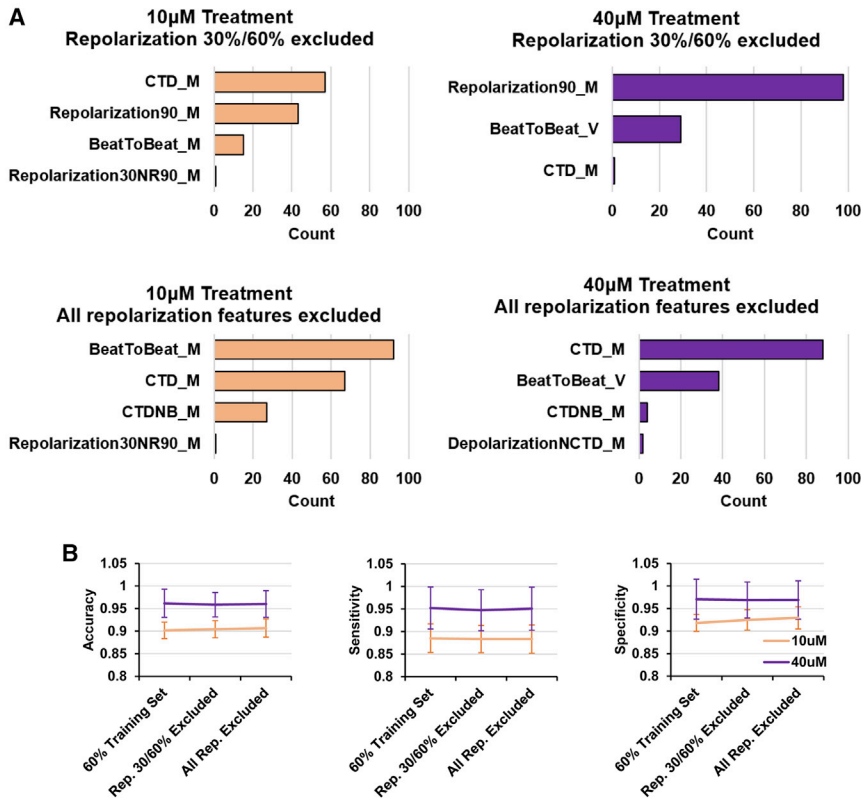


Figure 6. Secondary electrophysiological changes sufficiently recapitulate E4031 treatment arrhythmogenesis

(A) Total count of all parameters that scored >20 on the feature importance metrics across XGB models trained with reduced input variables. Top: repolarization 30% and 60% durations excluded. Bottom: all repolarization duration features excluded.

(B) Performance metrics of the XGB binary classifiers from the 60:40 train-test split compared with models trained with reduced input variables. Left: accuracy. Middle: sensitivity. Right: specificity. Mean \pm SD is plotted ($n = 100$ independent bootstraps).

generation of experimental groups, to include the CM electrophysiological data from patients associated with genetic risk factors, or exposed to other known transient risk factors (Myerburg et al., 1997). Simultaneously, additional experimental groups containing electrophysiological data from other sources of healthy CMs will also be required to overcome population level variability. As Ca^{2+} tracking of CMs is regularly used as a form of electrophysiological modeling across labs, future collaborative work and *post hoc* repurposing of experimental data will help build up a more extensive ML arrhythmia prediction platform.

Our developed video-processing pipeline is hassle free, automating away most of the tedium required to generate the large datasets required to train ML classifiers. Apart from manual fluorescence recordings and identification of single cells, all downstream processes are automated to generate the datasets. With the ability to generate large numbers of biological replicates of single CMs using hPSC technology, the whole process is of medium throughput. The process of repurposing other CM Ca^{2+} fluorescent videos from other research groups can also be streamlined.

With the current limitations on the reprogramming efficiency, patient-specific risk profiling and therapy via reprogramming and deriving CMs will be relatively slow.

The improvements to efficiency and next step for personalized medicine will likely occur when direct reprogramming of patient fibroblasts into CMs becomes reliable (Chen et al., 2017). Further improvements will then allow the rapid generation of patient CMs for the ML algorithm to make majority voting predictions for patient risk profiling. Therefore, this ML framework can directly be used to complement conventional, routine patient health check-ups and cardiovascular risk assessments to quantify arrhythmic risks in patients. Further automation for large-scale industrial drug screening can also complement current *in vitro* electrophysiological analysis and *in vivo* animal models. Scalability can be obtained by automation of CM derivation, fluorescent recording, and single-cell identification to drive high-throughput data generation. As such, CMs can be exposed to varying concentrations of drugs to conduct cardiotoxicity screens at scale, capturing more facets of possible arrhythmogenesis to improve the efficiency of preclinical studies. As the binary classification model has been shown to use biologically relevant parameters to separate healthy and arrhythmic CMs, it has the potential to be used as an unbiased tool to carry out hypothesis-generating research. Therefore, this study lays the groundwork and justification for future machine learning applications on electrophysiological data from CMs.



EXPERIMENTAL PROCEDURES

Fluorescent video capture of single CM Ca²⁺ cycles

Ca²⁺ cycles of CMs were imaged at 20× magnification using a Nikon ECLIPSE Ti-S fluorescent microscope and recorded using an Andor Zyla 4.2 sCMOS camera at 30 frames/s for 30 s. Ca²⁺ transients are detected as fluorescent emissions using a fluorescein isothiocyanate (FITC) filter cube. Video data were analyzed using Nikon's NIS-Elements AR to isolate single CMs as ROIs and obtain fluorescent intensity over time data for individual CMs per frame.

Video processing of fluorescence to compute Ca²⁺ handling parameters

Fluorescent intensity values were processed using our self-compiled code in R (RStudio version 1.2.1335/Base R version 3.6.3) to identify fluorescent peaks corresponding to single cardiac contractions. Individual Ca²⁺ transients were decomposed into a list of output parameters summarizing the shape of the transients mathematically, described in Table S1. Mathematical description of normalized parameters is provided in Table S2. Each sample was defined by the mean and SD of each parameter. For parameters describing absolute values (beat-to-beat duration, depolarization duration, repolarization duration, CTD), the relative SD (RSD) was calculated instead (RSD = SD/mean). All samples, classifications, and output parameters are assembled into datasets and are piped into the ML training algorithm.

Training ML classifiers to predict arrhythmogenesis and determine feature importance

The sample datasets are processed using self-compiled code in R using the caret library for supervised learning (Kuhn, 2015). ML algorithms trained were neural network (library nnet), random forest (library rf), extreme gradient boosting (library xgbTree) and support vector machine, radial kernel (library e1071) (Chang and Lin, 2011; Chen and Guestrin, 2016; Liaw and Wiener, 2002; Venables and Ripley, 2002). Each dataset described in the report is defined by a M × 17 matrix, with M corresponding to the number of individual CMs measured. Each CM is defined by 16 columns of parameters, as previously described, and assigned either “healthy” or the specific arrhythmic subtype classification.

Model training was done using the CaretList function with a tuneLength parameter of 18, except for XGB, which used a tuneLength parameter of 6. Multi-class classifiers were optimized using 10-fold cross-validation repeated three times for minimum logarithmic loss. Class predictions are made using the highest probability choice, and for the majority voting prediction strategy, all predictions were set to be the most common prediction across all CMs within each ROI. Performance of the classifiers was determined using the held-out datasets using the accuracy and kappa metrics. For the training of the XGB binary classifiers, optimization was done using 10-fold cross-validation repeated three times for maximum area under the operator curves. Performance of the classifiers were determined using the held-out datasets using the accuracy, sensitivity and specificity metrics. Feature importance of the built models was derived using the varImp function.

Data and code availability

All data are available in the main text or the supplemental information. Code used for fluorescence processing and ML is available at <https://github.com/Jemksp/Pang-Stem-Cell-Reports-2022>.

SUPPLEMENTAL INFORMATION

Supplemental information can be found online at <https://doi.org/10.1016/j.stemcr.2022.06.005>.

AUTHOR CONTRIBUTIONS

J.K.S.P. designed the research, cloned the plasmids, generated the GCaMP6s knockin lines, carried out the experiments, and ran the machine learning data analysis. J.K.S.P. and S.C. maintained the cells, generated the ANK2 mutant clones, and performed the single-cell Ca²⁺ video imaging. J.Z., P.S., and C.S. provided the HGPS lines and their expertise on HGPS. H.Y. gave guidance on the machine learning data analysis. W.-K.C., S.Y.N., and B.-S.S. supervised the project. J.K.S.P. and B.-S.S. wrote the manuscript.

CONFLICTS OF INTERESTS

The authors declare no competing interests.

ACKNOWLEDGMENTS

This work is supported by the Agency for Science, Technology and Research (Singapore) and by a grant to B.-S.S. (HBMS IAF-PP grant H19H6a0026). J.K.S.P. is supported by the National University of Singapore graduate scholarship.

Received: February 3, 2022

Revised: June 11, 2022

Accepted: June 13, 2022

Published: July 14, 2022

REFERENCES

- Adaniya, H., and Hiraoka, M. (1990). Effects of a novel class III anti-arrhythmic agent, E-4031, on reentrant tachycardias in rabbit right atrium. *J. Cardiovasc. Pharmacol.* *15*, 976–982. <https://doi.org/10.1097/00005344-199006000-00016>.
- Baker, R.E., Peña, J.M., Jayamohan, J., and Jérusalem, A. (2018). Mechanistic models versus machine learning, a fight worth fighting for the biological community? *Biol. Lett.* *14*, 20170660. <https://doi.org/10.1098/rsbl.2017.0660>.
- Bers, D. (2001). *Excitation-contraction Coupling and Cardiac Contractile Force* (Springer Science & Business Media).
- Brooks, A.R., Harkins, R.N., Wang, P., Qian, H.S., Liu, P., and Rubanyi, G.M. (2004). Transcriptional silencing is associated with extensive methylation of the CMV promoter following adenoviral gene delivery to muscle. *J. Gene Med.* *6*, 395–404. <https://doi.org/10.1002/jgm.516>.
- Ch'en, F.F.T., Vaughan-Jones, R.D., Clarke, K., and Noble, D. (1998). Modelling myocardial ischaemia and reperfusion. *Prog. Biophys. Mol. Biol.* *69*, 515–538. [https://doi.org/10.1016/S0079-6107\(98\)00023-6](https://doi.org/10.1016/S0079-6107(98)00023-6).



- Chang, C.-C., and Lin, C.-J. (2011). LIBSVM: a library for support vector machines. *ACM transactions on intelligent systems and technology (TIST)* 2, 1-27. [10.1145/1961189.1961199](https://doi.org/10.1145/1961189.1961199).
- Chen, T., and Guestrin, C. (2016). Xgboost: a scalable tree boosting system. Preprint at arXiv, 785–794. <https://doi.org/10.1145/2939672.2939785>.
- Chen, Y., Yang, Z., Zhao, Z.-A., and Shen, Z. (2017). Direct reprogramming of fibroblasts into cardiomyocytes. *Stem Cell Res. Ther.* 8, 118. <https://doi.org/10.1186/s13287-017-0569-3>.
- Clancy, C.E., and Rudy, Y. (1999). Linking a genetic defect to its cellular phenotype in a cardiac arrhythmia. *Nature* 400, 566–569. <https://doi.org/10.1038/23034>.
- Correia, C., Koshkin, A., Duarte, P., Hu, D., Teixeira, A., Domian, I., Serra, M., and Alves, P.M. (2017). Distinct carbon sources affect structural and functional maturation of cardiomyocytes derived from human pluripotent stem cells. *Sci. Rep.* 7, 8590. <https://doi.org/10.1038/s41598-017-08713-4>.
- Cunha, S.R., and Mohler, P.J. (2006). Cardiac ankyrins: essential components for development and maintenance of excitable membrane domains in heart. *Cardiovasc. Res.* 71, 22–29. <https://doi.org/10.1016/j.cardiores.2006.03.018>.
- Dempsey, G.T., Chaudhary, K.W., Atwater, N., Nguyen, C., Brown, B.S., McNeish, J.D., Cohen, A.E., and Kralj, J.M. (2016). Cardiotoxicity screening with simultaneous optogenetic pacing, voltage imaging and calcium imaging. *J. Pharmacol. Toxicol. Methods* 81, 240–250. <https://doi.org/10.1016/j.vascn.2016.05.003>.
- Fermini, B., Hancox, J.C., Abi-Gerges, N., Bridgland-Taylor, M., Chaudhary, K.W., Colatsky, T., Correll, K., Crumb, W., Damiano, B., Erdemli, G., et al. (2015). A new perspective in the field of cardiac safety testing through the comprehensive in vitro proarrhythmia assay paradigm. *J. Biomol. Screen* 21, 1–11. <https://doi.org/10.1177/1087057115594589>.
- Golgooni, Z., Mirsadeghi, S., Soleymani Baghshah, M., Ataee, P., Baharvand, H., Pahlavan, S., and Rabiee, H.R. (2019). Deep learning-based proarrhythmia analysis using field potentials recorded from human pluripotent stem cells derived cardiomyocytes. *IEEE J. Transl. Eng. Health Med.* 7, 1900203. <https://doi.org/10.1109/JTEHM.2019.2907945>.
- Harris, K., Aylott, M., Cui, Y., Louttit, J.B., McMahon, N.C., and Sridhar, A. (2013). Comparison of electrophysiological data from human-induced pluripotent stem cell-derived cardiomyocytes to functional preclinical safety assays. *Toxicol. Sci.* 134, 412–426. <https://doi.org/10.1093/toxsci/kft113>.
- Hayashi, M., Shimizu, W., and Albert, C.M. (2015). The spectrum of epidemiology underlying sudden cardiac death. *Circ. Res.* 116, 1887–1906. <https://doi.org/10.1161/CIRCRESAHA.116.304521>.
- Hennekam, R.C. (2006). Hutchinson–Gilford progeria syndrome: review of the phenotype. *Am. J. Med. Genet.* 140A, 2603–2624. <https://doi.org/10.1002/ajmg.a.31346>.
- Hwang, H., Liu, R., Maxwell, J.T., Yang, J., and Xu, C. (2020). Machine learning identifies abnormal Ca²⁺ transients in human induced pluripotent stem cell-derived cardiomyocytes. *Sci. Rep.* 10, 16977. <https://doi.org/10.1038/s41598-020-73801-x>.
- Ichikawa, M., Aiba, T., Ohno, S., Shigemizu, D., Ozawa, J., Sonoda, K., Fukuyama, M., Itoh, H., Miyamoto, Y., Tsunoda, T., et al. (2016). Phenotypic variability of ANK2 mutations in patients with inherited primary arrhythmia syndromes. *Circ. J.* 80, 2435–2442. <https://doi.org/10.1253/circj.cj-16-0486>.
- Jiang, Y., Zhou, Y., Bao, X., Chen, C., Randolph, L.N., Du, J., and Lian, X.L. (2018). An ultrasensitive calcium reporter system via CRISPR-Cas9-mediated genome editing in human pluripotent stem cells. *iScience* 9, 27–35. <https://doi.org/10.1016/j.isci.2018.10.007>.
- Juhola, M., Penttinen, K., Joutsijoki, H., Varpa, K., Saarikoski, J., Rasku, J., Siirtola, H., Iltanen, K., Laurikkala, J., Hyyrö, H., et al. (2015). Signal analysis and classification methods for the calcium transient data of stem cell-derived cardiomyocytes. *Comput. Biol. Med.* 61, 1–7. <https://doi.org/10.1016/j.compbiomed.2015.03.016>.
- Kuhn, M. (2015). Caret: classification and regression training. *Astrophysics Source Code Library*, ascl: 1505.1003.
- Kusumoto, D., and Yuasa, S. (2019). The application of convolutional neural network to stem cell biology. *Inflamm. Regen.* 39, 14. <https://doi.org/10.1186/s41232-019-0103-3>.
- Le Scouarnec, S., Bhasin, N., Vieyres, C., Hund, T.J., Cunha, S.R., Koval, O., Marionneau, C., Chen, B., Wu, Y., Demolombe, S., et al. (2008). Dysfunction in ankyrin-B-dependent ion channel and transporter targeting causes human sinus node disease. *Proc. Natl. Acad. Sci. USA* 105, 15617–15622. <https://doi.org/10.1073/pnas.0805500105>.
- Lian, X., Zhang, J., Azarin, S.M., Zhu, K., Hazeltine, L.B., Bao, X., Hsiao, C., Kamp, T.J., and Palecek, S.P. (2013). Directed cardiomyocyte differentiation from human pluripotent stem cells by modulating Wnt/ β -catenin signaling under fully defined conditions. *Nat. Protoc.* 8, 162–175. <https://doi.org/10.1038/nprot.2012.150>.
- Liaw, A., and Wiener, M. (2002). Classification and regression by randomForest. *R. News* 2, 18–22.
- Ma, J., Guo, L., Fiene, S.J., Anson, B.D., Thomson, J.A., Kamp, T.J., Kolaja, K.L., Swanson, B.J., and January, C.T. (2011). High purity human-induced pluripotent stem cell-derived cardiomyocytes: electrophysiological properties of action potentials and ionic currents. *Am. J. Physiol. Heart Circ. Physiol.* 301, H2006–H2017. <https://doi.org/10.1152/ajpheart.00694.2011>.
- Myerburg, R.J., Interian, A., Jr., Mitrani, R.M., Kessler, K.M., and Castellanos, A. (1997). Frequency of sudden cardiac death and profiles of risk. *Am. J. Cardiol.* 80, 10F–19F. [https://doi.org/10.1016/s0002-9149\(97\)00477-3](https://doi.org/10.1016/s0002-9149(97)00477-3).
- Oh, Y., Wei, H., Ma, D., Sun, X., and Liew, R. (2012). Clinical applications of patient-specific induced pluripotent stem cells in cardiovascular medicine. *Heart* 98, 443–449. <https://doi.org/10.1136/heartjnl-2011-301317>.
- Rivera-Torres, J., Calvo, C.J., Llach, A., Guzmán-Martínez, G., Caballero, R., González-Gómez, C., Jiménez-Borreguero, L.J., Guadix, J.A., Osorio, F.G., López-Otín, C., et al. (2016). Cardiac electrical defects in progeroid mice and Hutchinson–Gilford progeria syndrome patients with nuclear lamina alterations. *Proc. Natl. Acad. Sci. USA* 113, E7250–E7259. <https://doi.org/10.1073/pnas.1603754113>.
- Sallam, K., Li, Y., Sager, P.T., Houser, S.R., and Wu, J.C. (2015). Finding the rhythm of sudden cardiac death: new opportunities



- using induced pluripotent stem cell-derived cardiomyocytes. *Circ. Res.* *116*, 1989–2004. <https://doi.org/10.1161/CIRCRESAHA.116.304494>.
- Shin, H.Y., Wang, C., Lee, H.K., Yoo, K.H., Zeng, X., Kuhns, T., Yang, C.M., Mohr, T., Liu, C., and Hennighausen, L. (2017). CRISPR/Cas9 targeting events cause complex deletions and insertions at 17 sites in the mouse genome. *Nat. Commun.* *8*, 15464. <https://doi.org/10.1038/ncomms15464>.
- Simkin, D., Papakis, V., Bustos, B.I., Ambrosi, C.M., Ryan, S.J., Baru, V., Williams, L.A., Dempsey, G.T., McManus, O.B., Landers, J.E., et al. (2022). Homozygous might be hemizygous: CRISPR/Cas9 editing in iPSCs results in detrimental on-target defects that escape standard quality controls. *Stem Cell Rep.* *17*, 993–1008. <https://doi.org/10.1016/j.stemcr.2022.02.008>.
- Tallini, Y.N., Ohkura, M., Choi, B.-R., Ji, G., Imoto, K., Doran, R., Lee, J., Plan, P., Wilson, J., Xin, H.-B., et al. (2006). Imaging cellular signals in the heart in vivo: cardiac expression of the high-signal Ca²⁺ indicator GCaMP2. *Proc. Natl. Acad. Sci. USA* *103*, 4753–4758. <https://doi.org/10.1073/pnas.0509378103>.
- Varga, Z.V., Ferdinandy, P., Liaudet, L., and Pacher, P. (2015). Drug-induced mitochondrial dysfunction and cardiotoxicity. *Am. J. Physiol. Heart Circ. Physiol.* *309*, H1453–H1467. <https://doi.org/10.1152/ajpheart.00554.2015>.
- Venables, W., and Ripley, B. (2002). *Modern Applied Statistics, S*. Fourth, ed. (New York: Springer).
- Yap, Y.G., and Camm, A.J. (2003). Drug induced QT prolongation and torsades de pointes. *Heart* *89*, 1363–1372. <https://doi.org/10.1136/heart.89.11.1363>.
- Zhang, J., Lian, Q., Zhu, G., Zhou, F., Sui, L., Tan, C., Mutalif, R.A., Navasankari, R., Zhang, Y., Tse, H.-F., et al. (2011). A human iPSC model of Hutchinson Gilford progeria reveals vascular smooth muscle and mesenchymal stem cell defects. *Cell Stem Cell* *8*, 31–45. <https://doi.org/10.1016/j.stem.2010.12.002>.

Stem Cell Reports, Volume 17

Supplemental Information

Characterizing arrhythmia using machine learning analysis of Ca²⁺ cycling in human cardiomyocytes

Jeremy K.S. Pang, Sabrina Chia, Jinqiu Zhang, Piotr Szyniarowski, Colin Stewart, Henry Yang, Woon-Khiong Chan, Shi Yan Ng, and Boon-Seng Soh

Supplemental Materials

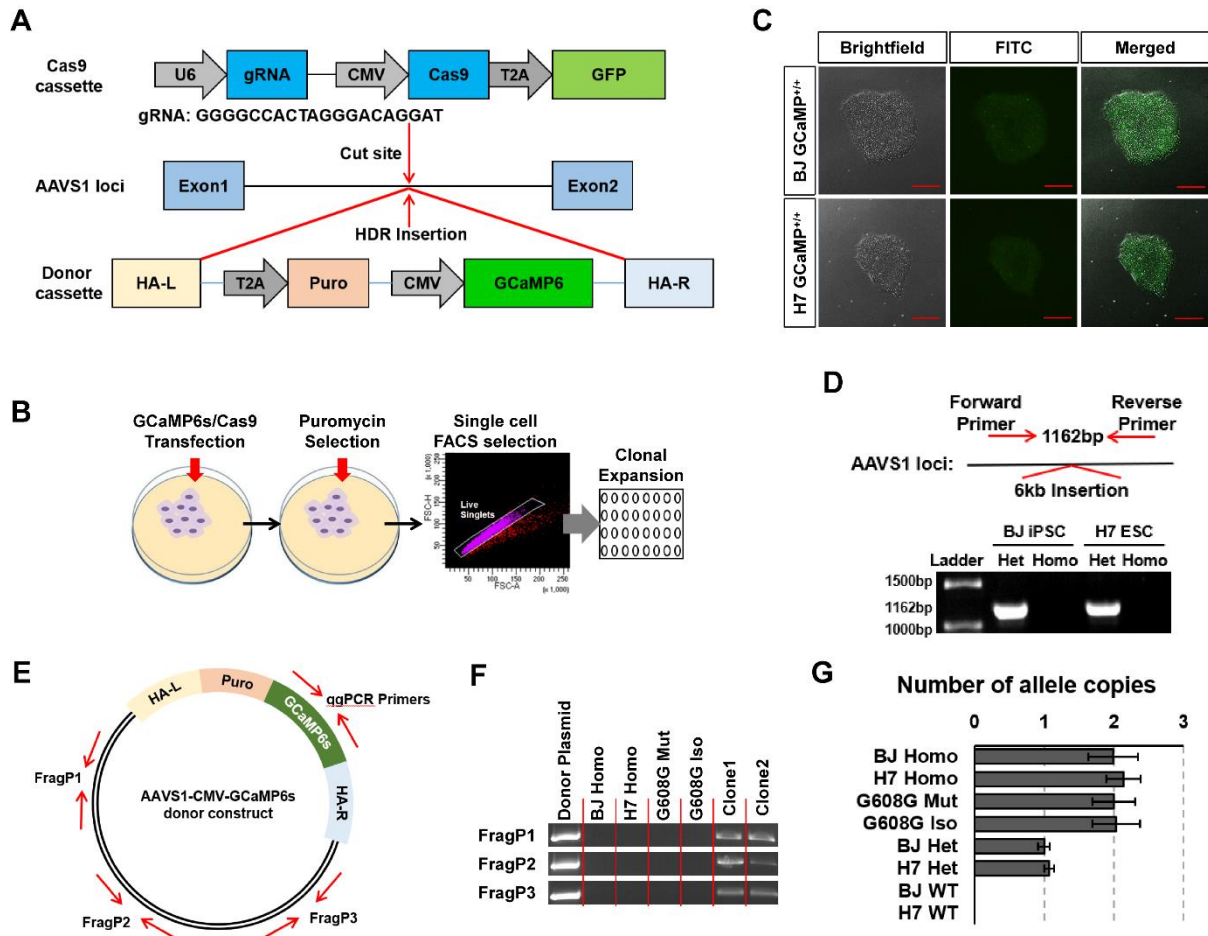
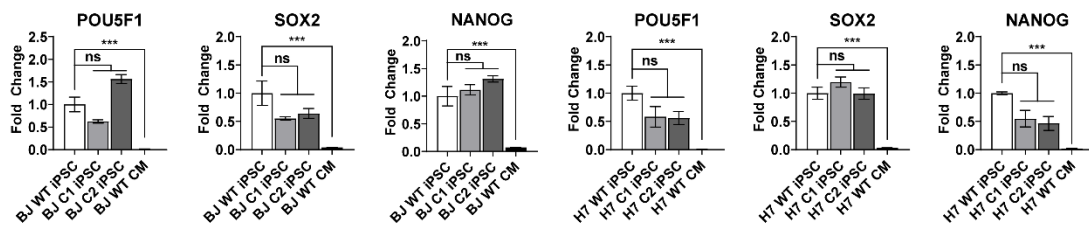
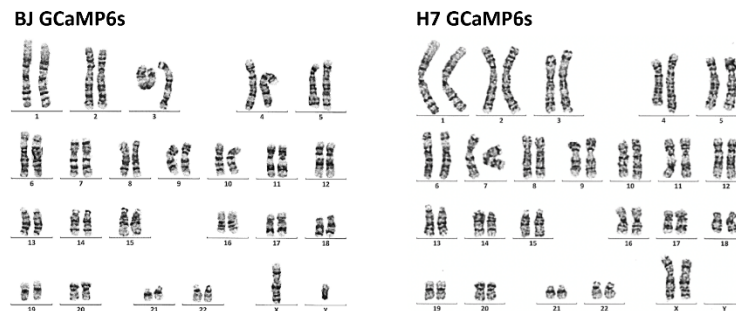


Figure S1: Related to Figure 2A for homozygous knock-in of GCaMP6s into hPSC lines
(A) Schematic representing the CRISPR-Cas9 strategy to insert the GCaMP6s sequence into the AAVS1 loci. **(B)** Efficient clonal isolation with successful insertions was achieved by puromycin selection followed by fluorescence activated cell sorting of single cells into individual wells. **(C)** Representative fluorescence images of hPSC clones with successful insertions. Constitutive GCaMP6s expression results in faint fluorescence in hPSCs observable under FITC filters. Scale bar = 200 μ m **(D)** Homozygous GCaMP6s insertion is confirmed using gel electrophoresis genotyping for the complete loss of the 1162bp amplicon spanning the insertion site. **(E)** Plasmid map denoting the primers used to PCR for plasmid fragments and the qgPCR primers used for allele copy number quantitative genotyping PCR. **(F)** PCR analysis for plasmid fragments of the GCaMP6s donor plasmid outside of the insertion cassette. Donor plasmid DNA was amplified as an amplification control (Lane 1). Clone1 and Clone2 were two positive control clones found to contain plasmid fragments (Lane 6 and 7). **(G)** GCaMP6s allele copy number quantitative genotyping PCR for the four parental lines used in this work (H7 Homo, BJ Homo, G608G Mut, G608G Iso), together with two heterozygous clones and the two WT hPSC lines. CT values were normalized to RELL2 as a stable housekeeping gene corresponding to 2 allele copies of a gene. Δ CT values were normalized to BJ Het to obtain $\Delta\Delta$ CT values corresponding to the number of allele copies of GCaMP6s insertions. Data is represented as Fold Change \pm SD (N = 3 technical replicates). BJ WT and H7 WT were undetected at a threshold of 40 cycles. **Het**, Heterozygous; **Homo**, Homozygous.

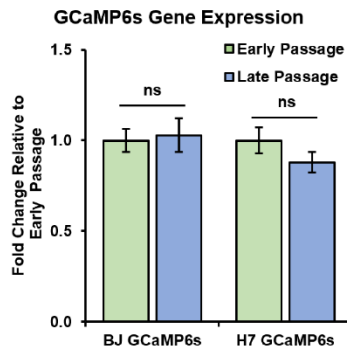
A



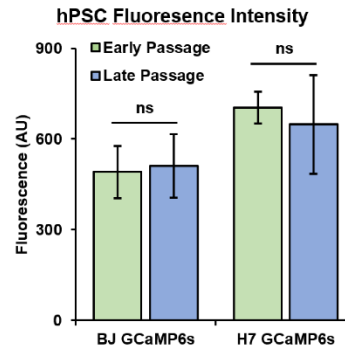
B



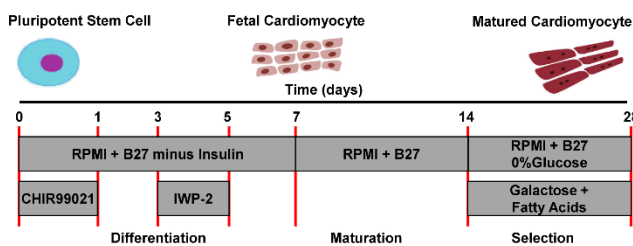
C



D



E



F

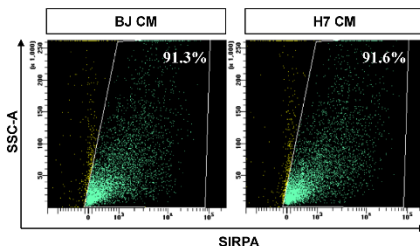


Figure S2: Related to Figure 2A for validation of successful generation of GCaMP6s expressing hPSC-CMs

(A) Quantitation of pluripotency gene expression levels for changes due to GCaMP6s insertion. Non-significant changes in both C1 (Heterozygous) and C2 (Homozygous) GCaMP6s insertions into BJ iPSCs (Left) or H7 ESCs (Right) confirms maintenance of pluripotency state. Comparison with differentiated CMs was included to highlight expected reduction in pluripotency gene expression when hPSCs leave the pluripotency state. $N = 3$ biological replicates; Mean \pm SD are plotted. *ACTB* is used as the housekeeping gene. Asterisks indicate statistical significance ($***P < 0.001$; ns, $P > 0.05$; two-tailed Students *t* test). **(B)** Karyotyping analysis for BJ GCaMP6s (Left) and H7 GCaMP6s (Right) lines. **(C)** Quantitative PCR comparison of GCaMP6s expression between Early (Passage < 10) and Late (Passage ~ 30) passage hPSCs post clonal isolation. $N = 3$ biological replicates; Mean \pm SD are plotted. *ACTB* is used as the housekeeping gene. Asterisks indicate statistical significance (ns, $P > 0.05$; two-tailed Students *t* test). **(D)** Fluorescence intensity quantification for hPSC lines in Early and Late passages post GCaMP6s insertion and clonal isolation. $N = 67$ colonies (BJ Lines) and $N = 26$ colonies (H7 Lines). **(E)** Directed CM differentiation and maturation protocol. **(F)** Representative flow cytometric analysis of Day 28 hPSC-CM representing matured, enriched CM populations.

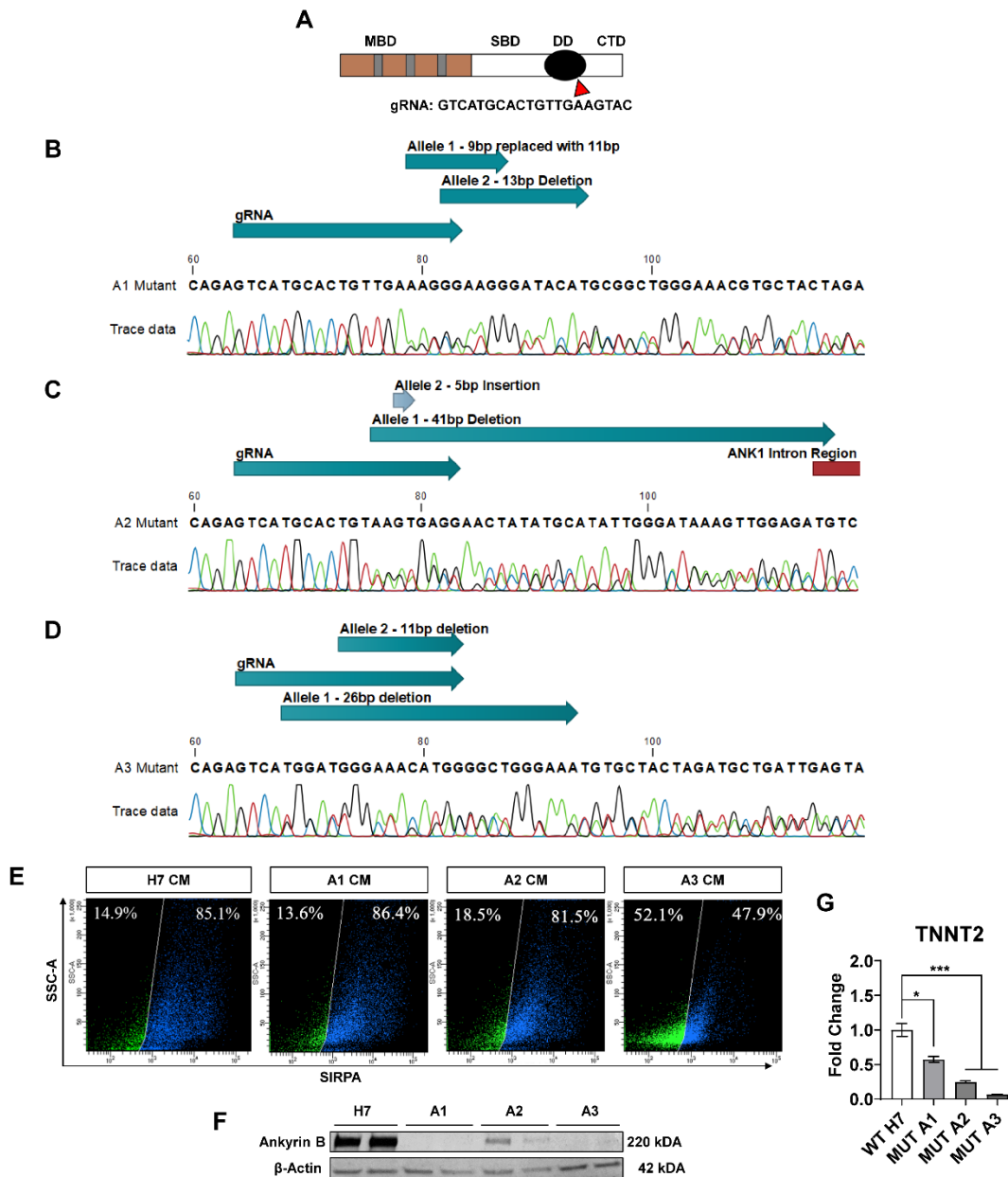
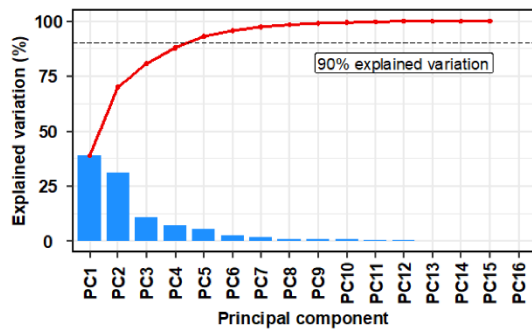
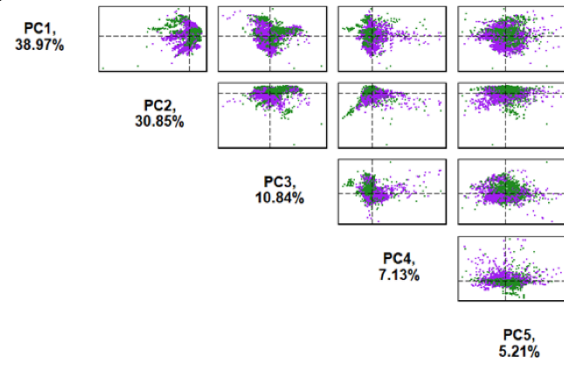


Figure S3: Related to Figure 3A for the characterising of AnkB mutant clones

(A) Schematic depicting the gRNA used to target Exon 40 of *ANK2* locus coding for the death domain of AnkB. Polymorphic mutations in the death domain and the C-Terminus domain have been linked with genetic dispositions to arrhythmias. **MBD**, Multiple Binding Domain; **SBD**, Spectrin Binding Domain; **DD**, Death Domain; **CTD**, C-Terminus Domain. (B to D), Sequencing data of the *ANK2* locus targeted by the gRNA for A1, A2 and A3 mutant lines respectively. For all three cell lines, biallelic frameshifts are expected. For A2 mutant, the 41bp Allele 1 deletion cuts into the following intronic region by 2 base pairs. Therefore, a 39bp deletion in-frame deletion of Exon 40 is expected, with a potential deletion of the splice domain. Exact insertion and deletion sequences are listed in Table S5. (E) Representative flow cytometry analysis of day 14 hESC-CMs before metabolic selection was done. (F) Western blot for AnkB protein expression in H7, A1, A2 and A3 day 28 hESC-CMs. Homozygous knock-outs are confirmed in A1 and A3 mutants, while heterozygous knock-out is confirmed in A2 mutant. (G) Quantitation of cardiomyocyte marker *TNNT2* expression levels showed significant reduction in expression for all three mutants confirming the poorer differentiation efficiency and maturation capabilities of the mutant CMs. $N = 3$ biological replicates; Mean \pm SD are plotted. *ACTB* is used as the housekeeping gene. Asterisks indicate statistical significance (** $P < 0.001$; * $P < 0.05$; two-tailed Student's t test).

A**B****Figure S5: Related to Figure 3B**

(A) Scree plot of the PCA shows that the first 5 PCs explains >90% of variation present. **(B)** Pairs plot showing the different combination pairs of the first 5 PCs. No clear distinction between healthy and arrhythmic classes can be observed.

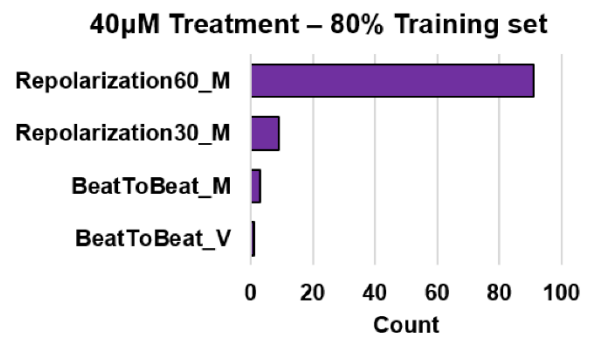
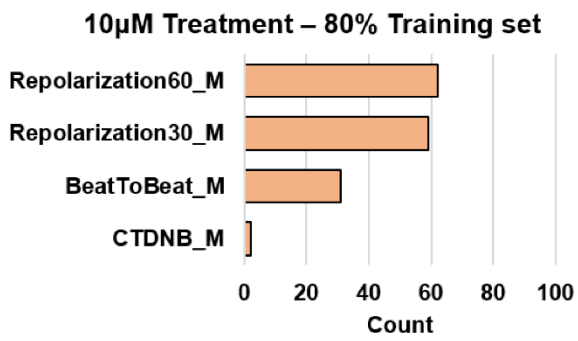
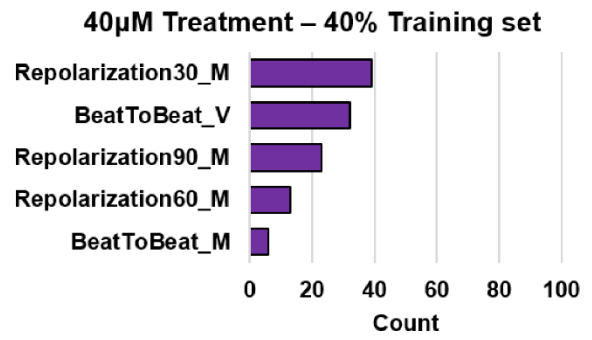
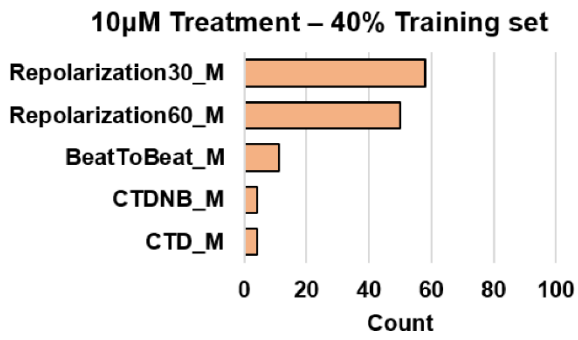


Figure S6: Related to Figure 5

Total count of all parameters that scored >20 on the feature importance metrics across XGB models trained using different train-test splits. **Top**, 40-60 train-test split; **Bottom**, 80-20 train-test split.

Table S1: Related to Results

Mathematical descriptors of individual Ca²⁺ transient parameters for a single contraction. All mathematical notation is defined similarly across different parameters.

Calcium transient parameters	Mathematical descriptor
Beat-To-Beat Duration T_{BTB}	$T_{BTB,i} = T_{Max,i+1} - T_{Max,i}$ Where $T_{Max,i}$ is the timestamp of the maximum intensity of a single contraction i
Depolarization Duration T_{DD}	$T_{DD,i} = T_{Max,i} - T_{Min,i}$ Where $T_{Min,i}$ is the timestamp of the minimum intensity of contraction i
Repolarization Duration $T_{R30 / R60 / R90}$ For 30%,60%,90% repolarization	$T_{R30/R60/R90,i} = T_{Int30/60/90,i} - T_{Max,i}$ $T_{Int30/60/90,i}$ is the timestamp of 30/60/90% reduction from the maximum intensity of contraction i
Calcium Transient Duration T_{CTD}	$T_{CTD,i} = T_{Int90,i} - T_{Min,i}$ Where T_i is the timestamp of contraction i

Table S2: Related to Results

Mathematical descriptors of normalized compound variables for a single contraction.

Compound Variables	Mathematical descriptor
Calcium Transient Duration Normalized to Beat to beat duration <i>CTD NB</i>	$CTD NB_i = \frac{T_{CTD,i}}{T_{BTB,i}}$ For a single contraction <i>i</i>
Depolarization Duration Normalized to Calcium Transient Duration <i>Depolarization NCTD</i>	$Depolarization NCTD_i = \frac{T_{DD,i}}{T_{CTD,i}}$ For a single contraction <i>i</i>
Repolarization 30% Duration Normalized to Repolarization 90% Duration <i>Repolarization30 NR90</i>	$Repolarization30 NR90_i = \frac{T_{R30,i}}{T_{R90,i}}$ For a single contraction <i>i</i>

Table S3: Related to Results

Theorized molecular explanations for the mean of each Ca²⁺ handling parameter of an individual cardiomyocyte

Parameter (Means)	Biological Meaning
Beat to Beat Duration Mean \bar{T}_{BTB}	How fast the cardiomyocytes are contracting. - Indicative of the pacing of the cardiomyocyte.
Depolarization Duration Mean \bar{T}_{DD}	Ca ²⁺ upstroke velocity. - Indicative of the duration Ca ²⁺ depolarization channels stay open.
Repolarization 30%, 60%, 90% Duration Mean $\bar{T}_{R30/R60/R90}$	Ca ²⁺ decay kinetics. - Indicative of the efficiency of the Ca ²⁺ repolarization channels, Ca ²⁺ -ATPase (SERCA) and Na ⁺ -Ca ²⁺ exchanger (NCX).
Calcium Transient Duration Mean \bar{T}_{CTD}	Entire duration that Ca ²⁺ is residing in the cytosol during a contraction.
Calcium Transient Duration normalized to Beat to Beat duration Mean $\bar{T}_{CTD NB}$	Proportion of the duration between contractions that the cardiomyocyte spends depolarized. - Larger ratios indicate shorter refractory periods between Ca ²⁺ releases
Depolarization Duration normalized to Calcium Transient Duration Mean $\bar{T}_{Depolarization NCTD}$	Proportion of a calcium transient corresponding to the depolarization phase. - Larger ratios indicate that a larger proportion of the calcium transient duration is spent depolarizing as opposed to repolarizing.
Repolarization Duration 30% normalized to 90% repolarization, Mean $\bar{T}_{Repolarization30 NR90}$	Indicative of Ca ²⁺ repolarization channels kinetics - Larger ratios indicate slower speed of Ca ²⁺ repolarization channels opening, resulting in a steeper sigmoidal function of the Ca ²⁺ decay.

Table S4: Related to Results

Theorized molecular explanations for the variation in each Ca²⁺ handling parameter of an individual cardiomyocyte

Parameter (Variations)	Biological Meaning
Beat to Beat Relative Standard Deviation RSD(T_{BTB})	Variation in the time difference between every contraction. - Indicative of the steady state of Ca ²⁺ flow.
Depolarization Duration Relative Standard Deviation RSD(T_{DD})	Variation in the Ca ²⁺ upstroke velocity. - Indicative of the steady state of Ca ²⁺ flow and the stability of Ca ²⁺ depolarization channels.
Repolarization 90% Duration Relative Standard Deviation RSD(T_{R90})	Variation in the Ca ²⁺ decay kinetics. - Indicative of the steady state of Ca ²⁺ flow with respect to Ca ²⁺ decay kinetics.
Calcium Transient Duration Relative Standard Deviation RSD(T_{CTD})	Variation of the entire duration that Ca ²⁺ is residing in the cytosol during a contraction. - Indicative of the steady state of Ca ²⁺ flow considering both Ca ²⁺ upstroke and decay.
Calcium Transient Duration normalized to Beat to Beat duration Standard Deviation SD($T_{CTD_{NB}}$)	Variation in the proportion of the duration between contractions that the cardiomyocyte spends depolarized. - Indicative of the steady state of Ca ²⁺ flow considering Ca ²⁺ refractory periods.
Depolarization Duration normalized to Calcium Transient Duration Standard Deviation SD($T_{Depolarization_{NCTD}}$)	Variation in the proportion of the Ca ²⁺ transient duration corresponding to the depolarization phase. - Indicative of the steady state of Ca ²⁺ flow considering both Ca ²⁺ upstroke and decay.
Repolarization Duration 30% normalized to 90% repolarization SD($T_{Repolarization_{NR90}}$)	Variation in Ca ²⁺ repolarization channel kinetics - Indicative of the steady state of Ca ²⁺ flow with respect to Ca ²⁺ decay kinetics.

Table S5: Related to Figure S3

Insertion and deletion mutagenesis regions for each of the alleles in the three AnkB mutants used in this manuscript

Cell Line	Mutation Region	Insertion	Deletion
Parental H7 WT	GTCATGCACTGTTGAAGTAC		
Ank1	Allele 1 GTCATGCACTGTTGA*AGTAC	GAGCAGAGGGT (9bp)	AGTACTGGC (11bp)
	Allele 2 GTCATGCACTGTTGAAGT*AC		ACTGGCTAGAGAG (13bp)
Ank2	Allele 1 GTCATGCACTGT*TGAAGTAC		TGAAGTACTGGCTAGAGAGGGATG GGAAACATGCTACAGGT (41bp)
	Allele 2 GTCATGCACTGTTGAAG*TAC	ACTAG (5bp)	
Ank3	Allele 1 GTCA*TGCACTGTTGAAGTAC		TGCACTGTTGAAGTAC TGGCTAGAGA (26bp)
	Allele 2 GTCATGCAC*TGTTGAAGTAC		TGTTGAAGTAC (11bp)

*Marks the beginning of the mutagenesis

GT in Ank2 Allele2 deletion is part of the intronic region

Table S6: Related to Experimental Procedures

List of DNA oligonucleotides used in this manuscript

DNA Oligonucleotide	Usage	5' to 3' Sequence
POU5F1 Forward Primer	qPCR (Fig. S2A)	TCAGCCAAACGACCATCTGCC
POU5F1 Reverse Primer		TTCTCTTTCGGGCCTGCACG
SOX2 Forward Primer		ATGCCTTCATGGTGTGGTCCC
SOX2 Reverse Primer		TCCGGGTGCTCCTTCATGTG
NANOG Forward Primer		AATGGTGTGACGCAGAAGGCC
NANOG Reverse Primer		TTGGAAGGTTCCCAGTCGGG
ACTB Forward Primer		CCCATCGAGCATGGTATCATC
ACTB Reverse Primer		AGAAGCATAACAGGGATAGCACT
TNNT2 Forward Primer	qPCR (Fig. S4C)	CAGAGCGGAAAAGTGGGAAGA
TNNT2 Reverse Primer		TCGTTGATCCTGTTTCGGAGA
GCaMP6s amplification Forward Primer	Cloning CMV-GCaMP6s (Fig. S1A)	TAGTTAGTCGACATGGGTTCTCATCATCA
GCaMP6s amplification Reverse Primer		ATATTAACGCGTTCACCTTCGCTGTCATC
AAVS1 gRNA Forward strand	Cloning CMV-GCaMP6s (Fig. S1A)	CACCGGGGGCCACTAGGGACAGGAT
AAVS1 gRNA Reverse strand		AAACATCCTGTCCCTAGTGGCCCCC
AAVS1 flanking Forward Primer	Genotyping Validation (Fig. S1D)	ATCCTCTCTGGCTCCATCGTA
AAVS1 flanking Reverse Primer		GCCATTGTCACTTTGCGCT
GCaMP6s qPCR Forward Primer	Genotyping Validation qPCR (Fig. S1G); Early/Late Passage qPCR (Fig. S2C)	ACCATGGTCGACTCATCACG
GCaMP6s qPCR Reverse Primer		TTCTTCTGCTTGTCGGCCTT
RELL1 Forward Primer	qPCR reference gene (Fig. S1G)	TGCTTGCTCAGAAGGAGCTT
RELL1 Reverse Primer		TGGGTTTCAGGAACAGAGACA
FragP1 Forward Primer	Plasmid fragment insertion PCR screen (Fig. S1F)	TCACTGGCCGTCGTTTTACA
FragP1 Reverse Primer		TCCCTTGTCCAGATAGCCCA
FragP2 Forward Primer		TGCCTGCTTGCCGAATATCA
FragP2 Reverse Primer		ATCTACACGACGGGGAGTCA
FragP3 Forward Primer		GGACAGGTATCCGGTAAGCG
FragP3 Reverse Primer		CCTGGGGTGCCTAATGAGTG
ANK2 gRNA Forward strand	ANK2 mutagenesis (Fig S3)	CACCGGTCATGCACTGTTGAAGTAC
ANK2 gRNA Reverse strand		AAACGTACTTCAACAGTGCATGACC
ANK2 sequencing Forward Primer	ANK2 Sequencing (Fig S3; Table S5)	TTTTGGAATCAAATGGGCCTG
ANK2 sequencing Reverse Primer		ACTGCAGATTAATGGCATTGCT
LMNA sequencing Forward Primer	LMNA Sequencing (Fig S4A)	CTCCCACTGCAGCAGCTC
LMNA sequencing Reverse Primer		GTGACCAGATTGTCCCCGAA

*gRNA target sequences are in **bold**

Supplemental Experimental Procedures

Maintenance of hPSCs

All hPSC lines used in this study were maintained feeder-free on Matrigel® matrix coated culture plates using StemMACS™ iPS-Brew XF containing 1X iPS-Brew XF supplement (Miltenyi Biotec, Germany) and 1% Penicillin/Streptomycin (Gibco, U.S.A.). Cells were maintained at 37°C under a humidified atmosphere with 5% CO₂. Passaging was done at 80-90% confluence using 1mg/ml Collagenase IV (Gibco, U.S.A). All experiments were performed with mycoplasma-free cells. H7 ESCs and BJ iPSCs were purchased from WiCell Research Institute. HGPS fibroblasts were purchased from NIA Aging tissue bank and reprogrammed into the HGPS line.

Transfection and clonal isolation of hPSCs

In preparation for transfection, hPSCs were dissociated using Accutase (Nacalai Tesque) at 37°C for 3 minutes and 250K cells were seeded overnight on single wells of a 6 well plate. The next day, plasmids were transfected into the seeded hPSCs using Lipofectamine™ Stem transfection reagent (Invitrogen™) at plasmid size dependent concentrations. For clonal isolation, hPSCs were dissociated using Accutase and resuspended in Phosphate Buffered Saline (PBS) containing 0.5% Fetal Bovine Serum (FBS), 1% Bovine Serum Albumin (BSA), 1% Penicillin/Streptomycin (Gibco, U.S.A.) and 5µM Y27632 (Miltenyi Biotec, Germany) and sorted into single wells using the LSR II (BD Biosciences, U.S.A).

GCaMP6s was stably knocked into each hPSC cell line using a Cas9 homology directed repair protocol described previously with slight modifications (Jiang et al., 2018; Ran et al., 2013). AAVS1 targeting gRNA was cloned into pSPCas9(BB)-2A-GFP (Addgene #48138; a gift from Feng Zhang). GCaMP6s donor plasmid was generated by inserting the GCaMP6s PCR amplicon from pGP-CMV-GCaMP6s (Addgene #40753; a gift from Douglas Kim & GENIE Project) into AAVS1-CAG-hrGFP (Addgene #52344; a gift from Su-Chun Zhang), replacing GFP. The optimized plasmid amounts used were AAVS1 gRNA plasmid containing Cas9 (0.6µg) and GCaMP6s donor plasmid (3.6µg) transfected with 10µL of Lipofectamine™ Stem in 2mL of iPS-Brew. Two days after transfection, cells were first selected using 1µg/ml puromycin for two days, and thereafter live cell sorted into single cells for clonal isolation.

A similar Cas9 directed mutagenesis was carried out to obtain the ANKB truncation clones (Ran *et al.*, 2013). ANKB targeting gRNA was cloned into pU6-(BbsI)_CBh-Cas9-T2A-mCherry (Addgene #64324; a gift from Ralf Kuehn). Disruption of the ANKB locus was first identified by PCR genotyping and confirmed using Sanger Sequencing. DNA oligonucleotide primers and gRNA sequences are listed in table S6. The optimized plasmid amount used for the ANKB gRNA plasmid containing Cas9 and mCherry was 0.7µg, transfected with 10µL of Lipofectamine™ Stem in 2mL of iPS-Brew. One day after transfection, the cells were live cell sorted, and cells positive for mCherry expression were sorted clonally into a 96 well plate for clonal expansion. Single clones were expanded until sufficient cells can be harvested for gDNA purification and downstream analysis. Disruption of the ANKB locus was first identified by PCR genotyping and confirmed using Sanger Sequencing. DNA oligonucleotide primers and gRNA sequences are listed in table S6.

Cardiomyocyte differentiation, selection and maturation

For differentiation, hPSCs were passaged in single cells using Accutase (Nacalai Tesque) and subjected to the previously established small molecule based GiWi cardiomyocyte differentiation protocol (Lian et al., 2013). At Day 7, the media was replaced with RPMI1640 (HyClone) containing 1X B27 with insulin supplement (Miltenyi Biotec) for maturation and refreshed every 2 days. At Day 14, the glucose level in the media was slowly reduced to 0% by Day 21, and the media was replaced with RPMI1640, 0% Glucose (HyClone), containing 1X B27 with insulin supplement, 100 µM Oleic Acid, 50 µM Palmitic Acid and 10mM Galactose to facilitate the metabolic maturation and selection of the cardiomyocytes to β-oxidation as described previously (Correia et al., 2017). On day 28, hPSC-CMs were used for Ca²⁺ imaging directly. For the drug-induced arrhythmogenesis dataset, BJ-CMs were treated with either DMSO as a vehicular control, 10µM or 40µM E4031 for 2 hours before Ca²⁺ imaging.

RNA extraction, reverse transcription and quantitative PCR

Cells were harvested in TRIzol (Invitrogen, U.S.A) and RNA was purified using Chloroform (Kanto Chemical, Japan) phase separation. 1 µg of purified RNA was reverse transcribed using High-Capacity cDNA Reverse Transcription Kit (Applied Biosystems, U.S.A.). Quantitative PCR was performed using FAST SYBR Green Mix (Applied Biosystems, U.S.A.), 0.3 µM of specific primers (Table S6) and ~5 ng of cDNA. $\Delta\Delta C_T$ -based relative quantification method was adopted for qPCR analysis using the QuantStudio 5 384-well Block Real-Time PCR system (Applied Biosystems, U.S.A.). The threshold cycle was determined to be 40. Data is presented as fold-change where CT values were normalised to *ACTB*.

Genomic DNA extraction, standard PCR and quantitative genotyping PCR

Cells were harvested using Accutase (Nacalai Tesque) and the genomic DNA was purified using Wizard® Genomic DNA Purification Kit (Promega) following manufacturer protocols. Standard PCR amplification was done using GoTaq® Green Master Mix (Promega). Quantitative genotyping PCR was carried out by adapting the protocol provided in (Simkin et al., 2022). Briefly, 1 µg of genomic DNA was digested to completion with EcoRI (NEB) and heat-inactivated at 65°C. ~10 ng of digested gDNA was loaded with 0.5 µM of qPCR primers into the FAST SYBR Green Mix (Applied Biosystems, U.S.A.) for quantitative PCR run. $\Delta\Delta C_T$ -based relative quantification method was adopted for qPCR analysis using the QuantStudio 5 384-well Block Real-Time PCR system (Applied Biosystems, U.S.A.). The threshold cycle was determined to be 40. ΔC_T values were normalized to *RELL2* as a stable housekeeping gene corresponding to 2 allele copies.

Protein extraction and western blot

Cells were harvested in RIPA buffer (ThermoScientific, U.S.A.) and protein quantification was carried out using Pierce™ BCA Protein Assay Kit (Thermo Scientific, U.S.A.). 30 ng of protein lysates were resolved in 8% SDS-PAGE gels in Tris-Glycine-SDS buffer before being transferred to PVDF membranes (Bio-Rad, U.S.A) for probing with specific antibodies and imaging using Clarity™ ECL Western Substrate (Bio-Rad, U.S.A). Primary antibodies used are as follows: anti-AnkB mouse (1:200; Abcam; ab131419), anti-LMNA/C mouse (1:500; Abcam; ab40567), anti-β-actin mouse (1:1000; Cell Signaling Technology, 3700S), anti-GAPDH rabbit (1:2500; Abcam; ab9485). Secondary antibodies conjugated with horseradish peroxidase (1:1000; Santa Cruz Biotechnology, U.S.A; sc-516102) were used.

Fluorescent cytometric analysis

hPSC-CMs were dissociated in a similar manner to hPSCs described above. CMs were stained with anti-human CD172a/b (SIRPα/β) conjugated antibody (1:300; Biolegend; #323808) for 1 hour in PBS containing 1% FBS. The cells were washed thoroughly and resuspended in PBS containing 0.5% FBS and 1% BSA for flow cytometric analysis performed using LSR II (BD Biosciences, U.S.A.).

Statistical analysis

All statistical analysis were performed using R. Students *t* test was used to compare quantitative gene expression results and all parameters across treatment groups in each ML dataset. All tests were two-tailed, and $P < 0.05$ were considered significant.

Supplemental References

Correia, C., Koshkin, A., Duarte, P., Hu, D., Teixeira, A., Domian, I., Serra, M., and Alves, P.M. (2017). Distinct carbon sources affect structural and functional maturation of cardiomyocytes derived from human pluripotent stem cells. *Scientific Reports* 7, 8590. 10.1038/s41598-017-08713-4.

Jiang, Y., Zhou, Y., Bao, X., Chen, C., Randolph, L.N., Du, J., and Lian, X.L. (2018). An Ultrasensitive Calcium Reporter System via CRISPR-Cas9-Mediated Genome Editing in Human Pluripotent Stem Cells. *iScience* 9, 27-35. 10.1016/j.isci.2018.10.007.

Lian, X., Zhang, J., Azarin, S.M., Zhu, K., Hazeltine, L.B., Bao, X., Hsiao, C., Kamp, T.J., and Palecek, S.P. (2013). Directed cardiomyocyte differentiation from human pluripotent stem cells by modulating Wnt/ β -catenin signaling under fully defined conditions. *Nat Protoc* 8, 162-175. 10.1038/nprot.2012.150.

Ran, F.A., Hsu, P.D., Wright, J., Agarwala, V., Scott, D.A., and Zhang, F. (2013). Genome engineering using the CRISPR-Cas9 system. *Nat Protoc* 8, 2281-2308. 10.1038/nprot.2013.143.

Simkin, D., Papakis, V., Bustos, B.I., Ambrosi, C.M., Ryan, S.J., Baru, V., Williams, L.A., Dempsey, G.T., McManus, O.B., Landers, J.E., et al. (2022). Homozygous might be hemizygous: CRISPR/Cas9 editing in iPSCs results in detrimental on-target defects that escape standard quality controls. *Stem Cell Reports* 17, 993-1008. <https://doi.org/10.1016/j.stemcr.2022.02.008>.